



HAL
open science

Classification and dynamic assessment of droop-based grid-forming control schemes: Application in HVDC systems

Ebrahim Rokrok, Taoufik Qoria, Antoine Bruyere, Bruno Francois, Xavier Guillaud

► **To cite this version:**

Ebrahim Rokrok, Taoufik Qoria, Antoine Bruyere, Bruno Francois, Xavier Guillaud. Classification and dynamic assessment of droop-based grid-forming control schemes: Application in HVDC systems. Electric Power Systems Research, 2020, 189, pp.106765 -. 10.1016/j.epsr.2020.106765 . hal-03492380

HAL Id: hal-03492380

<https://hal.science/hal-03492380>

Submitted on 22 Aug 2022

HAL is a multi-disciplinary open access archive for the deposit and dissemination of scientific research documents, whether they are published or not. The documents may come from teaching and research institutions in France or abroad, or from public or private research centers.

L'archive ouverte pluridisciplinaire **HAL**, est destinée au dépôt et à la diffusion de documents scientifiques de niveau recherche, publiés ou non, émanant des établissements d'enseignement et de recherche français ou étrangers, des laboratoires publics ou privés.



Distributed under a Creative Commons Attribution - NonCommercial 4.0 International License

16 **Abstract**

17 Ordered mesoporous silica SBA-15 and KIT-6 supported Ni/ZrO₂ catalysts are evaluated
18 for the hydrodeoxygenation of guaiacol (stirred batch reactor, 300 °C, 50 bar of H₂),
19 guaiacol being a model compound of bio-oil issued from the lignin fraction of biomass
20 liquefaction step. ZrO₂ and Ni are dispersed using incipient-wetness impregnation (IWI) or
21 two-solvent (TS) method over mesoporous silica. Mesoporous zirconia (nanocasting
22 method) and conventional zirconia were also used as supports. Cyclohexane, cyclohexanol
23 and methoxycyclohexanol are the main products of reaction. Significant differences in
24 cyclohexane yield are measured (after 8 h reaction, with conversion in most cases above
25 85%): NiZr-KIT-TS, 71.6% > NiZr-SBA-TS, 63.3% >> Ni/meso-Zr, 7.8% > NiZr-SBA-
26 IWI, 5.2% > Ni/ZrO₂, 1.6%. Tetragonal ZrO₂ phase, acting as oxophilic phase for guaiacol
27 / oxygenated intermediates adsorption and activation, is observed whatever the approach
28 selected for the preparation. However, when nickel is supported over pure zirconia, low
29 selectivity to cyclohexane is obtained, while the main product becomes cyclohexanol with
30 yields reaching ~40%. Better activities and selectivities toward total deoxygenation
31 (cyclohexane production) are obtained for the silica supported Ni-ZrO₂ catalysts, especially
32 when the catalyst is prepared by the two-solvent approach. Improvement is associated to
33 the proximity between Ni and ZrO₂ particles when confined in the silica mesopores.
34 Finally, conversion and yield to cyclohexane obtained with NiZr-KIT-TS are stable during
35 5 successive catalytic cycles demonstrating the absence of significant modification of the
36 catalyst during reaction. These results are evidencing that the confining strategy is efficient
37 to improve stability of active elements during HDO reaction.

38

39

40 **Keywords:** ZrO₂; Ni; mesoporous silica; hydrodeoxygenation; guaiacol; biomass.

41

42 **1. Introduction**

43 Lignocellulosic biomass is a renewable and abundant feedstock, considered as an important
44 raw resource for the biorefineries. Thermal and thermochemical processes are sustainable
45 methods for producing bio-oils, from which chemicals and fuels can be obtained [1, 2].
46 Bio-oils are composed of a significant fraction of oxygenated aromatic compounds (up to
47 40%) [3], having a high potential for the production of chemical derivatives [4].
48 Unfortunately, the aromatic nature and the high oxygen content of the raw bio-oil results in
49 inadequate properties for a direct fuel valorisation (high viscosity, high acidity, low
50 stability, low heating value [5-7]). Oxygen content decrease is a key step in the upgrading
51 of the lignocellulosic derived bio-oil, in order to obtain valuable products such as alkanes
52 and aromatics. Among the different available processes, the catalytic hydrodeoxygenation
53 (HDO) has gained considerable attention during the past two decades. HDO reaction is
54 generally conducted at temperatures between 150 and 500 °C, and under H₂ pressure (up to
55 3 MPa), in the presence of a heterogeneous catalyst [8-10]. Considering the severe reaction
56 conditions, and the production of water and CO/CO₂ (reaction products), robust catalysts
57 are needed [11].

58 HDO studies are often conducted over model compounds such as guaiacol, anisole and
59 other phenolic compounds [12, 13]. Guaiacol, 2-methoxyphenol, is an oxygenated
60 compound representative of the phenolic fraction contained in bio-oils derived from lignin
61 [12, 14, 15]. Besides, the cleavage of the aromatic methoxy group and of the hydroxy group
62 of guaiacol (both major functional groups of lignin-derived phenolic compounds) is
63 complex since the reactivity of products under the applied reaction conditions can lead to
64 polymerization reactions, and consequently organic matter accumulation on the catalyst
65 surface [16] that causes catalyst deactivation. Consequently, high selectivity in
66 deoxygenated compounds can be obtained only under careful control of operational
67 parameters and catalyst properties [16, 17]. Among the catalyst functions needed, metal
68 phase acts for hydrogen activation but metal only is not sufficient to obtain satisfying
69 selectivities to deoxygenated compounds. Acid / oxophilic sites are also needed to improve
70 deoxygenated products selectivities, and can also lead to an activity increase [18-20].
71 Sulfided MoS₂, CoMo-S, NiMo-S (hydrotreating catalysts) [21-25] and unsupported /

72 supported (SiO_2 , Al_2O_3 , activated carbon, TiO_2 , ZrO_2 or zeolites) metal nitrides such as
73 Mo_2N [26, 27] were then proposed for the reaction. Over sulphide catalysts, the presence of
74 oxygen and water led to rapid catalyst deactivation [21, 22, 24]. Sulfur-containing
75 molecules (dimethyldisulfide (DMDS), H_2S) has to be added in the reaction feed to obtain
76 better stability [21, 28, 29]. Supported noble metals - Pt, Pd, Ir, Ru or Rh - are also
77 effective catalysts [30-32], as well as Ni [31-34]. Using acidic catalysts (containing both
78 Brønsted or Lewis sites) allows to modulate reaction selectivity with these metals [30, 35-
79 37], inhibiting hydrogenation of oxygenated intermediates [35] or achieving complete
80 deoxygenation [30, 36]. Aromatic ring, bearing oxygenated functional groups, is adsorbed
81 and activated on the oxophilic / acidic surfaces, in orientations favoring the C-O bond
82 activation and breaking [18, 21, 37-39]. According to different theoretical models, supports
83 like SiO_2 favors adsorption of phenol ring on three different modes i) π -interaction, ii) flat
84 O-interaction and iii) perpendicular O-interaction, although the adsorption mode depends
85 on the surface structure of the silica [40]. For instance, on Fe/SiO_2 catalyst, H_2 molecule is
86 dissociatively adsorbed on metallic Fe sites while guaiacol [41] or phenol [40] is adsorbed
87 on closest silanol groups of weak acidity to be hydrogenated. For several catalyst
88 formulations, stability remains a drawback. Using monometallic or bimetallic noble metal-
89 based catalysts, rapid catalyst deactivation generally occurs [21, 42-44]. Carbon
90 accumulation is, in part, at the origin of the activity decrease [45], and active phase
91 sintering [46], accumulation of oxygen containing molecules on catalyst surface [46] are
92 other identified reasons. In addition to Ni, non-noble metals such as Cu [47], Mo [48, 49]
93 and Fe [41, 50], in addition to transition metal phosphides [51, 52] and carbides [53] were
94 also proposed as alternative catalysts. While the metals always promote the hydrogenation
95 reactions, Lewis or Brønsted [37, 54]; presence of oxophilic surface sites (Zr^{4+} , Ti^{4+}) [55,
96 56], the metal itself (case of Ni [57]); the oxygen surface vacancies density affording C-O
97 bond activation [58-60].

98 Among the possible supports, transition alumina is not enough stable toward water [61].
99 ZrO_2 or TiO_2 appear more appropriate due to oxophilic surface properties, but commercial
100 supports exhibit low surface areas which is detrimental to the dispersion of active metals
101 [62]. An open stable porosity is preferable [63], a characteristic which fits with ordered
102 mesostructured materials. Among, some of them exhibit satisfying hydrothermal stability

103 [64-66]. Additionally, the presence of large mesopores is also favorable to reactant
104 diffusion to active sites, leading to efficient mass transfer [67, 68]. As aforementioned,
105 silica is an adequate support for HDO reaction, considering that the amorphous silica
106 surface of low silanol concentration will ensure a catalyst suffering from limited inhibition
107 by water and CO, while phenolic compounds will adsorb on surface silanol in favorable
108 configuration [40, 69]. HDO of vanillin was then reported using 5 wt.% Pd/KIT-6 [68]. A
109 98% vanillin conversion with 94% selectivity toward p-cresol (300 °C, 6 h, flow = 50 mL
110 min⁻¹, WHSV of 21.2 h⁻¹) is reported. HDO of anisole was also studied over Ni/SBA-15 or
111 Co/SBA-15, Ni-based catalyst exhibiting high selectivity toward methoxycyclohexane
112 (~80%) at complete anisole conversion (300 °C, 10 bar of H₂) [70]. Al-modified silica also
113 presents adequate surface properties. Over Pt/Al-SBA-15 (Si/Al = 20), 70% guaiacol
114 conversion with a 43% cyclohexane yield (250 °C for 2 h, 400 rpm, 40 bar of H₂) was
115 reported by Yu et al. [71]. Rh-Ni over Al-KIT-6 silica is also an efficient catalyst for the
116 HDO of diphenyl ether and guaiacol [72]. Literature dealing with non-siliceous mesoporous
117 materials as supports in HDO reaction is rather more limited [73].

118 In this work, ordered mesoporous silica SBA-15 and KIT-6 were used as supports to
119 disperse Ni-ZrO₂ particles, and to prepare mesoporous ZrO₂ supported Ni catalyst.
120 Catalysts were tested for the HDO of guaiacol reaction, a model oxygenated molecule of
121 lignin-derived bio-oil. The results show that the approach selected for the deposition of Ni
122 and ZrO₂ phases is of paramount importance. High selectivity toward cyclohexane (~80%)
123 at high guaiacol conversion (>90%) can then be obtained over silica composites prepared
124 by the two-solvent impregnation approach.

125 **2. Experimental**

126 **2.1. Mesoporous SBA-15 and KIT-6 silica support synthesis**

127 SBA-15 silica was synthesized using classical hydrothermal procedure, using the nonionic
128 triblock copolymer surfactant P123 (PEO20-PPO70-PEO20, MW = 5800 g mol⁻¹, BASF)
129 [74, 75]. 12.0 g of P123 were dissolved in a solution containing 360 g of ultrapure water
130 and 37.2 g of concentrated hydrochloric acid (37 wt.%). The solution was heated at 35 °C.
131 24.0 g of tetraethyl orthosilicate (TEOS, Merck, 98%) were added, and the mixture was

132 aged at 35 °C during 24 h. Then, the suspension was hydrothermally treated at 140 °C
133 during 24 h. The solid was recovered by filtration without washing, air-drying at 80 °C, and
134 final calcination at 550 °C for 3 h under static air (heating rate = 1 °C min⁻¹).

135 KIT-6 silica was synthesized, using the same soft template, P123 [76]. 6.0 g of P123
136 surfactant were dissolved in a solution containing 217 g of ultrapure water and 11.7 g of
137 concentrated hydrochloric acid (37 wt.%) at 35 °C. Thereafter, 6.0 g of 1-butanol (Merck,
138 99%) were added and the resulting solution was stirred for 1 h before the addition of 12.9 g
139 of TEOS. The resulting solution was aged at 35 °C during 24 h, and hydrothermally treated
140 at 100 °C during 24 h. Recovery and activation procedures were exactly the same than
141 applied for the SBA-15 support.

142 **2.2. Preparation of silica supported Ni-ZrO₂ catalysts**

143 Impregnation of ZrO₂ and NiO in the silica supports was performed using two different
144 impregnation procedures: (i) Incipient-Wetness Impregnation, IWI, leading to NiZr-SBA-
145 IWI catalyst; (ii) Two-Solvents impregnation [77], TS, leading to NiZr-SBA-TS and NiZr-
146 KIT-TS. The nominal Zr and Ni loadings were 15 and 10 wt.%, respectively.

147 *Case of IWI procedure:* aqueous solutions were prepared for nickel (S1) and zirconium (S2)
148 precursors. Solution S1 was prepared by dissolving Ni(NO₃)₂·6H₂O (Sigma–Aldrich,
149 ≥98.5%, p.a. grade) and solution S2 by dissolving ZrO(CO₃)·xH₂O (Amuco Inc. ≥40%
150 ZrO₂) in water. Solution S2 was slowly dropped onto 2.0 g of freshly calcined SBA-15
151 support. After homogenization, the solid was dried at 80 °C during 12 h and finally
152 calcined under static air at 700 °C (temperature increase rate = 2 °C min⁻¹). In a second
153 step, solution S1 was slowly dropped onto the Zr-SBA support. In both cases, the volume
154 of solution used for the impregnation corresponded to the pore volume of the powders as
155 measured by N₂ physisorption. Finally, the solid was dried at 80 °C for 12 h and was
156 calcined under static air at 700 °C (temperature increase rate = 2 °C min⁻¹).

157 *Case of TS procedure:* 2.0 g of the freshly calcined silica (SBA or KIT) were dispersed in
158 70 mL of pentane (J.T. Baker, analysis reagent, ≥98%,) by stirring during 15 min.
159 Thereafter, aqueous precursor solution (prepared by dissolving ZrO(CO₃)·xH₂O (Amuco
160 Inc. ≥40% ZrO₂) in water) was added dropwise to the pentane containing silica. The

161 volume of water added corresponded to 1/2 of the support pore volume as measured by N₂-
162 physisorption, in which calculated mass of zirconium precursor was dissolved. The powder
163 was recovered by filtration, dried at 80 °C for 12 h and calcined under static air at 700 °C
164 for 1 h (temperature heating rate = 2 °C min⁻¹). Step of nickel impregnation was performed
165 using an exactly similar procedure, dissolving the mass of Ni(NO₃)₂·6H₂O (Sigma–Aldrich,
166 ≥98.5%, p.a. grade) in water. For final activation, the catalyst is calcined under static air at
167 700 °C.

168 The catalysts were named as follow: NiZr-S-IMP, where S indicated the support name
169 (SBA or KIT) and IMP indicated the selected method of impregnation, TS or IWI.

170 **2.3. Preparation of ZrO₂ supported Ni catalyst**

171 Mesoporous ZrO₂ (meso-Zr) was synthesized using nanocasting approach, using SBA-15
172 silica as hard template [78]. Firstly, the silica powder was dispersed in an excess of organic
173 solvent (pentane). Secondly, silica porosity was filled with 1.2 mL of an aqueous solution
174 containing the zirconium precursor, ZrO(CO₃)·xH₂O. The resulting mixture was
175 magnetically stirred for 30 min at room temperature. The powder was recovered by
176 filtration, air-drying at 80 °C for 24 h, and calcination at 700 °C for 1 h (temperature
177 heating rate = 2 °C min⁻¹). The procedure was repeated a second time in order to increase
178 zirconia loading. Finally, the silica matrix was removed by dissolution (12 h under stirring),
179 using a NaOH solution (0.2 M; 10 mL per g of solid), followed by water washing and
180 drying at 80 °C. The procedure was repeated two times to ensure a >95 wt% silica removal.
181 Ni/ZrO₂ (Ni/meso-Zr) was prepared using IWI procedure, using Ni(NO₃)₂·6H₂O precursor.
182 After impregnation, the powder was dried at 90 °C for 12 h, and calcined at 700 °C for 1 h
183 (temperature heating rate = 2 °C min⁻¹).

184 For comparison, a catalyst was prepared using a conventional ZrO₂ support, obtained by
185 thermal decomposition of the zirconium precursor, ZrO(CO₃)·xH₂O, at 700 °C (1 h ;
186 temperature heating rate = 2 °C min⁻¹). The impregnation of nickel precursor solution was
187 performed using IWI procedure. This catalyst was named as Ni/ZrO₂.

188 **2.4. Characterization methods**

189 Inductively Coupled Plasma - Optical Emission Spectrometry (ICP-OES) was performed to
190 determine the elemental composition of catalysts (Ni, Zr and Si), using a 720-ES ICP-OES
191 Agilent instrument with axially viewing and simultaneous CCD detection. The wavelengths
192 used were: 221.320 nm (Ni), 267.865 nm (Zr) and 198.863 nm (Si). For analysis, a known
193 mass of catalyst (10.0 mg) was dissolved in 1 mL of concentrated HF solution and 2 mL of
194 concentrated *aqua regia* solution. The samples were heated up to 110 °C (Vulcan digester).
195 Then, 4 mL of UNS-1 solution (Inorganic Ventures) were added to deactivate HF and to
196 maintain solubility of the sample through complexation. Finally, samples were diluted up to
197 20 mL in water.

198 N₂ adsorption-desorption isotherms were recorded at 77 K on an ASAP2010 instrument
199 from Micromeritics. Before each analysis, the sample was degassed at 250 °C during 12 h
200 (residual pressure < 0.00667 mbar). The Brunauer-Emmett-Teller (BET) method was
201 applied to calculate the specific surface area. The Barrett-Joyner-Halenda (BJH) method
202 was applied on the adsorption branch to determine the pore size distribution and the mean
203 pore size value. Total pore volume was estimated on the adsorption branch, at a P/P₀ value
204 of 0.95.

205 Powder XRD patterns were obtained using a Bruker AXS D8 advanced X-Ray
206 diffractometer equipped with a CuK α ($\lambda = 1.54184 \text{ \AA}$) anticathode and a Lynxeye xe-t type
207 detector (operating at 40 kV and 40 mA). Diffractograms were recorded for 2θ from 10 to
208 80°, with steps of 0.02° (step time of 2 min). For low-angle analysis, the diffractograms
209 were collected in the reflection mode in the 2θ range from 0.5 to 5° with a step of 0.02°
210 (step time of 2 s).

211 Morphology of catalysts was evaluated using Scanning Electron Microscopy (SEM), with a
212 JEOL JSM-6490 LV instrument. For analysis, samples were fixed on a graphite ribbon, and
213 surface was coated with gold for analysis (using a DENTON VACUUM Desk IV
214 equipment). The microscope was equipped with an EDX detector, allowing to perform
215 element mapping on material surface. To determine active phase dispersion, samples were
216 characterized by Transmission Electron Microscopy (TEM). Images were recorded on a
217 Tecnai F20 Super Twin TMP instrument. For analysis, samples were embedded in a resin
218 and cut into ~100 nm width slices using an EM UC7 LEICA ultramicrotome.

219 X-ray Photoelectron Spectroscopy (XPS) was performed over calcined samples, before
220 reduction step. The spectra were recorded on a KRATOS Analytical AXIS Ultra^{DLD}
221 spectrometer equipped with a charge neutralizer. The analysis was made under an ultrahigh
222 vacuum of $\sim 5 \times 10^{-9}$ Torr. X-ray were produced by an aluminium anode operating with Al
223 K_{α} source (1486.6 eV) at 15 kV. The binding energy (BE) values were referred using the
224 binding energy peak of Si 2p at 103.5 eV [79]. The surface Zr/Si, Ni/Si, Ni/Zr and Si/O
225 atomic ratios were calculated using the CASA XPS software, after subtracting a nonlinear
226 Shirley background.

227 Dihydrogen Temperature Programmed Reduction (H_2 -TPR) analysis was performed on an
228 AUTOCHEM 2920 Micromeritics analyzer, equipped with a thermal conductivity detector
229 (TCD). For each experiment, 50 mg of catalyst were pretreated at 400 °C under helium
230 flowing (50 mL min^{-1}) for 1 h. Thereafter, the sample was cooled down to 35 °C and heated
231 under H_2 flow (5.0 vol.% H_2 diluted in Ar, total flow rate of 50 mL min^{-1}) from 40 °C to
232 900 °C, applying a temperature increase rate of 10 °C min^{-1} . H_2 concentration variation is
233 registered online on the TCD, affording to quantify the extent of material reduction.

234 NH_3 -TPD analysis was carried out on a Micromeritics AUTOCHEM 2910 equipment,
235 equipped with a TCD detector, and coupled with a mass spectrometer for NH_3
236 quantification. The samples (100.0 mg) were pretreated under He flow (30 mL min^{-1}) at
237 400 °C for 1 h, and the samples were cooled down to 35 °C. Thereafter, the samples were
238 heated under H_2 flow (5.0 vol.% H_2 in Ar, total flow rate = 50 mL min^{-1}) from 40 °C to 450
239 °C (heating rate of 10 °C min^{-1}). Finally, the solids were exposed to a flow containing 10
240 vol.% NH_3 in He (30 mL min^{-1}) for 30 min at 100 °C. The physisorbed ammonia was
241 purged with He (30 mL min^{-1}) for 1 h. NH_3 desorption was measured, applying a
242 temperature increase rate of 5 °C min^{-1} up to 700 °C under a He flow (30 mL min^{-1}). The
243 temperature is maintained at 700 °C during 1 h to ensure the TCD baseline return to its
244 initial value. The NH_3 concentration was on line monitored on a Pfeiffer vacuum
245 OmniStarTM GSD301 mass spectrometer, allowing, after integration of the signal, to
246 determine the total NH_3 amount desorbed during the cycle.

247 **2.5. HDO of guaiacol catalytic reaction**

248 Guaiacol catalytic hydrodeoxygenation reaction was performed in a stainless-steel batch
 249 reactor (OGAWA, 25 mL). Prior to the reaction, the catalysts were reduced at 450 °C for 2
 250 h (temperature increase rate of 5 °C min⁻¹) under H₂ (total flow rate = 50 mL min⁻¹).
 251 Hexadecane is selected as solvent for the reaction, since the use of non-polar solvent
 252 favored hydrogenation of the aromatic ring by leading to a coplanar adsorption of the
 253 aromatic ring on the catalyst surface. In polar solvents, the vertical adsorption of the
 254 reactants through the hydroxyl group is favored [80-82]. The absence of external and
 255 internal mass transfer limitations was also confirmed in the conditions of reaction applied
 256 with the solvent selected. The details of the procedure were reported in a previous paper
 257 [83]. The mass transfer limitations were evaluated using the Weisz-Prater (C_WP) and
 258 Mears Criterion (C_M). The estimated C_WP and C_M values were below 1 and 0.15,
 259 respectively, indicating that internal pore diffusion and external diffusion limitations were
 260 negligible. To conclude, under selected reaction conditions, the reaction was not controlled
 261 by diffusional effects.

262 For each experiment, 17.5 mL of guaiacol solution (0.6 mol L⁻¹) in hexadecane and 0.1 g of
 263 catalyst were added into the reactor, which was thereafter sealed and purged under H₂. The
 264 reactor temperature was set at 300 °C. When temperature reached 300 °C, stirring rate was
 265 stabilized at 600 rpm and 5 MPa of H₂ was added into the reactor. Reaction ended after 8 h.
 266 Liquid products were analyzed using a gas chromatograph (GC, Shimadzu QP2010 Ultra)
 267 equipped with a flame ionization detector and a DB-5 capillary column (30 m x 0.25 mm x
 268 0.10 μm) for product separation. Tetradecane was selected as internal standard. Liquid
 269 samples were also analyzed using mass spectrometry to identify organic compounds
 270 present.

271 Conversion and product yields were calculated as follow:

$$272 \text{ Conversion of guaiacol, } C_{GUA}(\%) = \frac{n_{GUA, in} - n_{GUA, out}}{n_{GUA, in}} \times 100; \quad \text{Yield, } Y_{product i}(\%) =$$

$$273 \frac{n_{product i}}{n_{GUA, in}} \times 100; \text{ Where } n_{GUA, in} \text{ is the initial number of moles of guaiacol, } n_{GUA, out} \text{ is}$$

274 the final number of moles of guaiacol, $n_{product i}$ is the number of moles of the i^{th} product
 275 formed in the liquid phase.

276 Carbon balance was calculated as follow: *Carbon balance, C_{balance} (%) =*

$$277 \frac{\sum n_{C, product i} + n_{GUA, out}}{n_{GUA, in}} \times 100. \text{ Where } \sum n_{C, product i} \text{ is the sum of number of moles of C in}$$

278 each identified product. Gas phase analysis is performed by Gas Chromatography. The
279 detailed procedure is presented in ESI file.

280 Catalytic tests were performed two times to ensure reproducibility of the results.
281 Conversion and selectivity presented are the average values of the two tests. The standard
282 deviation for all reported data is 2%.

283 3. Results and discussion

284 3.1. Catalyst composition

285 Catalysts composition was determined using ICP analysis (Table 1). The results showed
286 that nickel contents vary from 7.7 to 11.0 wt.%, depending on the preparation method. The
287 experimental Zr loading was measured at values from 10.1 to 11.4 wt.%. Silicon content in
288 Ni/meso-Zr was also determined, since silicon is a residue from the nanocasting synthesis
289 to produce the mesoporous zirconia. A value of 1.9 wt.% of Si was determined, indicating
290 that the approach adopted ensured an almost complete dissolution of the initial silica
291 template.

292

293 **Table 1.** Catalyst composition and selected textural properties of supports and catalysts.

Sample	Ni content (wt.%)	Zr content (wt.%)	V_p ($\text{cm}^3 \text{g}^{-1}$)	ΔV_p^a (%)	S_{BET} ($\text{m}^2 \text{g}^{-1}$)	ΔS_{BET}^a (%)	d_{BJH} (nm)
SBA-15	---	---	1.20	---	520	---	11.4
NiZr-SBA-IWI	7.7	10.1	0.82	31	347	33	9.7
NiZr-SBA-TS	11.0	10.6	0.86	28	363	30	9.8
KIT-6	---	---	1.20	---	830	---	6.7
NiZr-KIT-TS	9.7	11.4	0.63	47	462	44	6.2
Meso-Zr	---	---	0.40	---	204	---	4.9; 7.5
Ni/meso-Zr	8.7	---	0.28	30	141	31	4.6; 7.3

294 ^a loss proportion after deposition of the nickel and zirconium phases.

295

296 3.2. Textural and structural characterization

297 The results of nitrogen adsorption-desorption characterization are gathered in Table 1.
298 Isotherms and pore size distribution are presented in Figure S1. Isotherms for SBA-15,
299 KIT-6 silica supports, as well as for NiZr-based catalysts, are of type IV (Fig. S1), a shape
300 characteristic of mesoporous materials [84]. SBA-15 support presented H1 type hysteresis,
301 with parallel and vertical adsorption and desorption branches. This isotherm is
302 characteristic of ordered mesoporous supports having narrow pore size distribution and
303 cylindrical pores. For KIT-6, while the isotherm remains of type IV, the hysteresis shifted
304 between H1 and H2, H2 being observed for mesoporous materials presenting
305 interconnected mesopores.

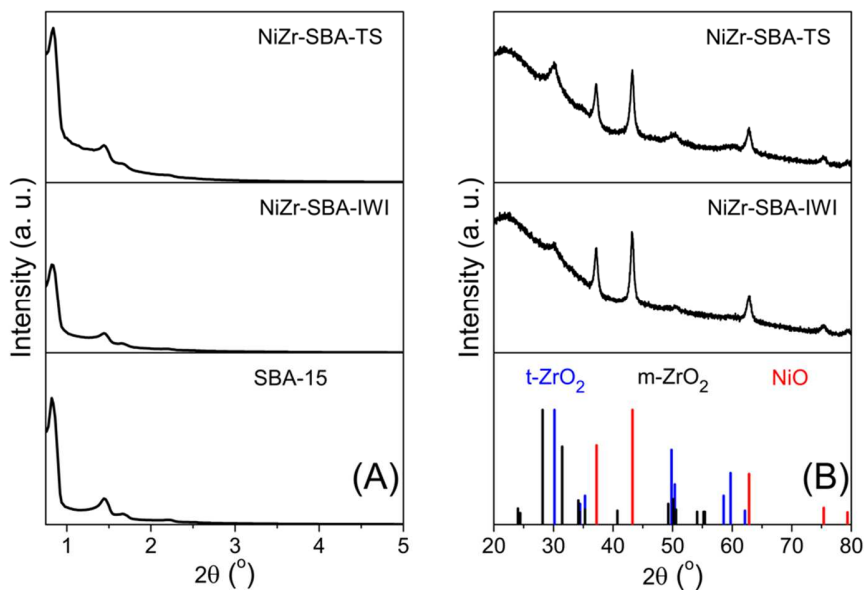
306 After impregnation and calcination for the obtaining of NiO and ZrO₂ supported
307 nanoparticles, no significant modification of isotherm and hysteresis shapes are observed
308 (Fig. S1). Proportions of pore volume and surface area decrease after NiO and ZrO₂
309 formations are listed in Table 1. Over SBA-15 support, no notable effect of the
310 impregnation route (TS, IWI) can be noted on the extent of pore volume decrease, which is
311 for both catalysts around 30%. More important decrease in pore volume was observed over
312 KIT-6 derived catalyst (47%). For most of the catalysts, the decrease in surface area is
313 comparable with that of the pore volume: ~ 30% over SBA-15; ~ 44% over KIT-6. Finally,
314 the limited changes in pore size distribution and mean pore size value (with a maximum of
315 pore size decrease of 15% in the case of NiZr-SBA materials) is showing a limited
316 modification of the pore structures upon impregnation - drying - calcination cycle. Results
317 obtained however suggest that NPs (NiO and ZrO₂) are formed in the support mesopores,
318 resulting in a consequent pore filling (reflected by pore volume and surface area decreases,
319 and a limited pore size change). For meso-Zr and Ni/meso-Zr (Fig. S1), isotherm of type IV
320 is obtained, with, however, a larger pore size distribution obtained. These results clearly
321 demonstrate a less periodic mesopore structure on the long-range order in these materials,
322 as compared with the silica supports. Surface area of 204 m² g⁻¹ is obtained for the meso-
323 Zr, a value that is decreasing by 31% after impregnation cycle and calcination for NiO
324 formation. Comparable decrease in pore volume is measured.

325 Low-angle XRD patterns for SBA-15 and NiZr-SBA catalysts are shown in Figure 1. All
326 diffractograms displayed one main peak located at $2\theta \sim 0.82^\circ$ and two additional peaks of
327 lower intensity located at $2\theta \sim 1.44^\circ$ and 1.68° (Fig. 1A). Identified reflections are ascribed

328 to the (100), (110) and (200) planes of the ordered pore structure of hexagonal symmetry
 329 (space group $P6mm$) [74]. Results confirm that the impregnation procedures (IWI or TS) do
 330 not induce any significant alteration of the long-range ordering in the SBA-15 silica, as
 331 deduced from the maintaining of comparable isotherms shape and hysteresis. Similar
 332 results were obtained for KIT-6 based materials (Fig. 2A), with diffraction peaks located at
 333 $2\theta \sim 0.98^\circ$, 1.16° and 1.9° , ascribed to the (211), (200) and (332) reflections of the cubic
 334 structure of $Ia3d$ symmetry [76]. For meso-Zr and Ni/meso-Zr (Fig. 3A), low-angle
 335 reflections were poorly defined compared to those recorded over the ordered silica
 336 containing solids. The main peak, of highest intensity and characteristic of the (100) plan
 337 was located at $2\theta \sim 0.88^\circ$, while a second broad signal was observed at 1.40° . Although
 338 they were not well resolved, they indicated the formation of a periodic mesoporous
 339 structure, the broadening of the signal being often observed over non-siliceous oxides
 340 produced by nanocasting [85, 86].

341

342



343

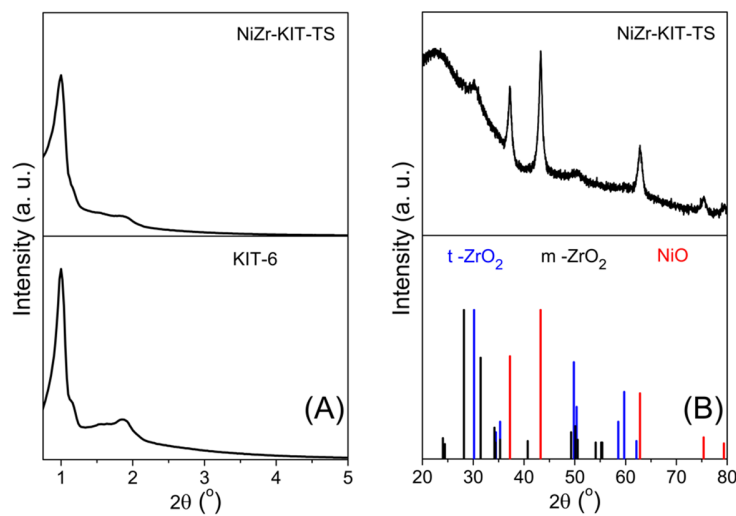
344 **Figure 1.** (A) Low-angle X-ray diffraction patterns for: SBA-15, NiZr-SBA-IWI, NiZr-
 345 SBA-TS; (B) wide-angle X-ray diffraction patterns for: NiZr-SBA-IWI, NiZr-SBA-TS.

346

347 Diffractograms recorded for 2θ values between 20° and 80° are presented in Figure 1 to
348 Figure 3. Reflections located at $2\theta \sim 30.1^\circ$, 35.1° , 50.1° and 60.0° are characteristic of
349 tetragonal ZrO_2 phase (JCPDS file n°17-0923). Only tetragonal phase is observed to form
350 in materials containing impregnated ZrO_2 phase, and even over meso-Zr. In nickel
351 containing solids, additional reflections located at $2\theta \sim 37.2^\circ$, 43.3° , 62.9° , 75.4° and 79.3°
352 are observed. These reflections are characteristic of NiO phase (PDF file n°01-073-1523).

353

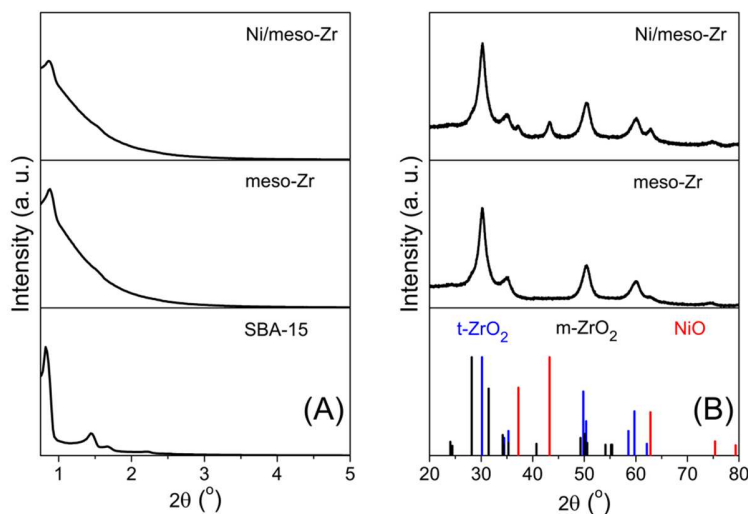
354



355

356 **Figure 2.** (A) Low-angle X-ray diffraction patterns for: KIT-6, NiZr-KIT-TS; (B) wide-
357 angle X-ray diffraction patterns for: NiZr-KIT-TS.

358



359

360 **Figure 3.** (A) Low-angle X-ray diffraction patterns for: SBA-15, meso-Zr, Ni/meso-Zr; (B)
 361 wide-angle X-ray diffraction patterns for: meso-Zr and Ni/meso-Zr.

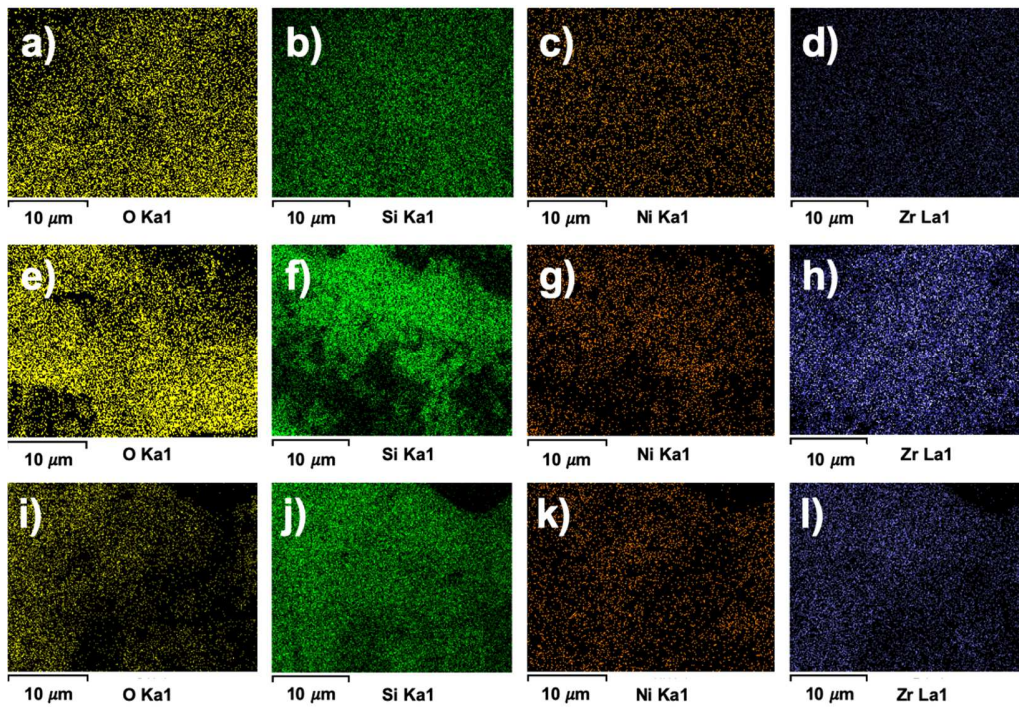
362

363 3.3. Morphology characterization

364 SEM images obtained for Ni-ZrO₂ supported catalysts are shown in Figure S2. For SBA-
 365 based catalysts (NiZr-SBA-TS in Fig. S2a), silica particles exhibited a rope-like shape
 366 forming string-like aggregates. This is a classical morphology observed for SBA-15 type
 367 support [87, 88]. NiZr-KIT-TS (Fig. S2b) showed particles without a defined shape and
 368 wide-open spaces visible on the surface. Finally, images of the Ni/meso-Zr (Fig. S2c)
 369 showed characteristic, although not uniform, string-like aggregates, comparable to that of
 370 the SBA-15 used as hard-template. It indicates that the morphology of the silica template
 371 determines the morphology of the ZrO₂ particles obtained by nanocasting.

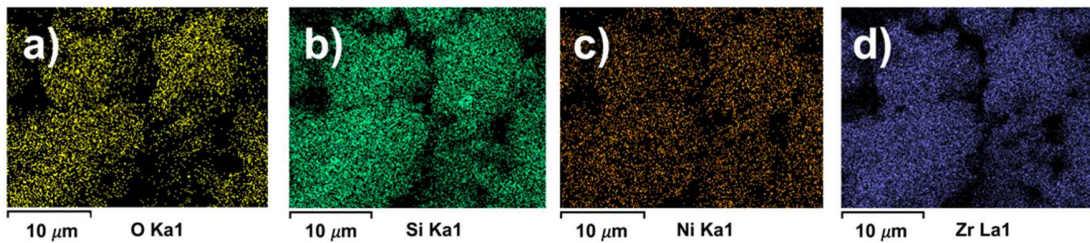
372 Macroscopic dispersion of elements was evaluated by EDX-mapping (Fig. 4 and Fig. 5 for
 373 calcined catalysts; Fig. 6 for reduced catalyst). No evident segregation of Ni and Zr through
 374 the whole areas analyzed can be observed. These results indicate a satisfying dispersion of
 375 elements issued from the impregnation process. For the Ni/meso-Zr catalyst, silicon is also
 376 detected at low intensity (Fig. 5) in accordance to ICP analysis result confirming the
 377 presence of residual silica template in the final material. After reduction of NiZr-KIT-TS
 378 sample (Fig. 6), EDX-mapping showed no significant sintering of the elements, with Si, Zr
 379 and Ni species always observed to be well-distributed in the whole analyzed areas.

380



381

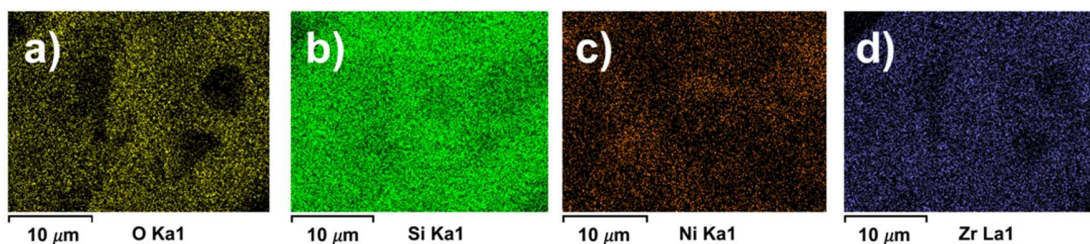
382 **Figure 4.** SEM EDX analyses. Oxygen in yellow, Silicon in green, Nickel in brown and
383 Zirconium in blue for a-b-c-d) NiZr-SBA-IWI, e-f-g-h) NiZr-SBA-TS and i-j-k-l) NiZr-
384 KIT-TS.



385

386 **Figure 5.** SEM EDX analyses. Oxygen in yellow, Silicon in green, Nickel in brown and
387 Zirconium in blue for Ni/meso-Zr.

388



389

390 **Figure 6.** SEM EDX analysis. Oxygen in yellow, Silicon in green, Nickel in brown and
391 Zirconium in blue for reduced NiZr-KIT-TS sample (450 °C, 2 h).

392

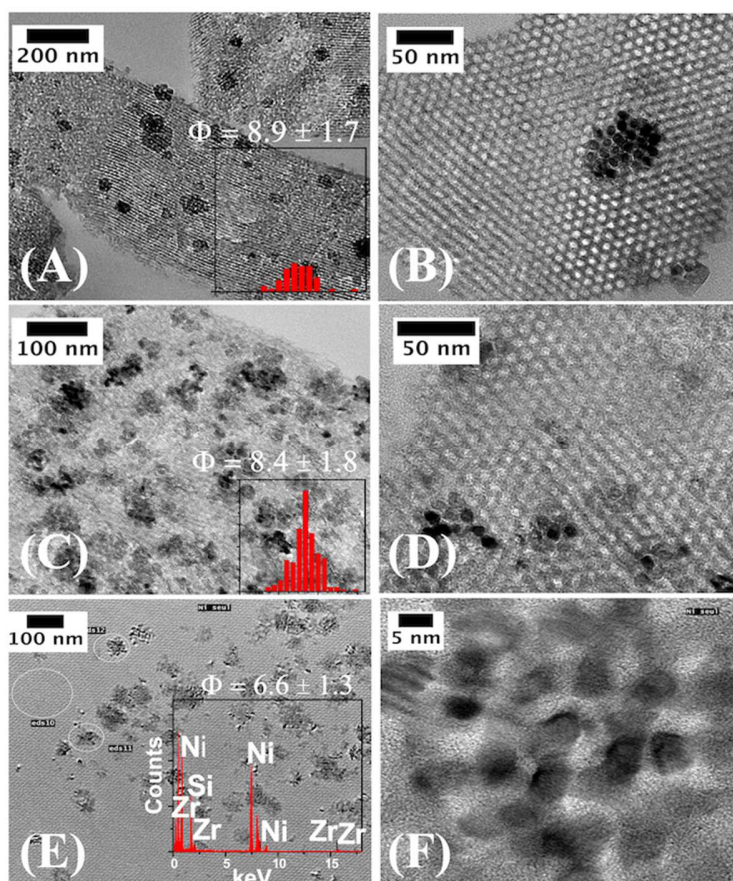
393 Transmission electron microscopy was performed to determine Ni- and Zr-containing
394 phases localization and size. TEM images obtained for NiZr-SBA and NiZr-KIT catalysts
395 are presented in Figure 7. Support mesopores of uniform size are clearly observed,
396 confirming the preservation of the pore structure after impregnation - activation cycle (as
397 deduced from N₂-physisorption and low angle XRD experiments). Such retaining of initial
398 pore structure was observed regardless of the impregnation method (IWI, TS) and silica
399 support type (SBA, KIT). Then, the observed decrease in textural parameters (Table 1, 30
400 to 40% of the initial values) can be attributed to pore clogging more than to pore collapse.
401 Indeed, NiO and/or ZrO₂ nanoparticles were observed to form confined within the pores.
402 This observation is valid for both IWI and TS-derived catalysts. The presence of a few
403 proportion of external particles, of larger size (30-50 nm) as visible in Figure 7, was
404 detected for all impregnated materials and whatever the impregnation route adopted. The
405 crystalline character of the obtained particles is supported by visible lattice fringes at high
406 magnification (Fig. 8). The indexation of the diffraction patterns obtained on such
407 crystallized particles allowed to confirm the presence of tetragonal ZrO₂ (lattice planes
408 spacing in agreement with JCPDS n°17-0923) and NiO (lattice planes spacing in agreement
409 with JCPDS n°01-073-1523).

410 The IWI procedure resulted in the formation of mesopore confined nanoparticles (NPs)
411 with diameter of 8.9 ± 1.7 nm (Fig. 7), a diameter value close to the mesopore diameter of
412 the parent SBA-15 (Table 1). Formation of NPs assemblies of elementary NPs in the
413 mesopores, linked together by the connecting secondary pore network of the SBA-15, was
414 observed, as already reported [89, 90]. Due to the assembly between adjacent mesopores of
415 several NPs to form pseudo-aggregates of various sizes, some of them exceeding tenths of
416 nanometers, an inhomogeneous repartition of the impregnated oxides was observed
417 throughout the silica grain porosity. Focused EDX analysis evidenced formation of Ni-rich
418 aggregates (from pure nickel) to Zr-rich aggregates (from pure zirconia). However, large-
419 zone analyses (silica grain scale) showed Ni and Zr loadings close to the expected values.
420 In the case of the TS approach, formation of mesopore confined NPs (Fig. 7-8) was also

421 observed, but with a reduced size of the assemblies formed between the adjacent mesopores
422 and a better metal oxide distribution within the mesopores of the support is obtained
423 (whatever the support morphology, SBA-15 or KIT-6). The average NPs size in NiZr-SBA-
424 TS reached 8.4 ± 1.8 nm, value close to the mesopore diameter of the parent SBA-15
425 (Table 1). For NiZr-KIT-TS, average NPs size of 6.6 ± 1.3 nm was obtained, a value in
426 agreement with the pore diameter of the silica KIT-6 support. To conclude, NiO and ZrO₂
427 particles confined in the mesopores of SBA-15 and KIT-6 silica supports form when
428 catalysts are prepared by the IWI and TS approach. Confining of NPs results in pore
429 plugging that can explain the evolutions in textural parameters as observed for the surface
430 area and pore volume evolutions.

431

432



433

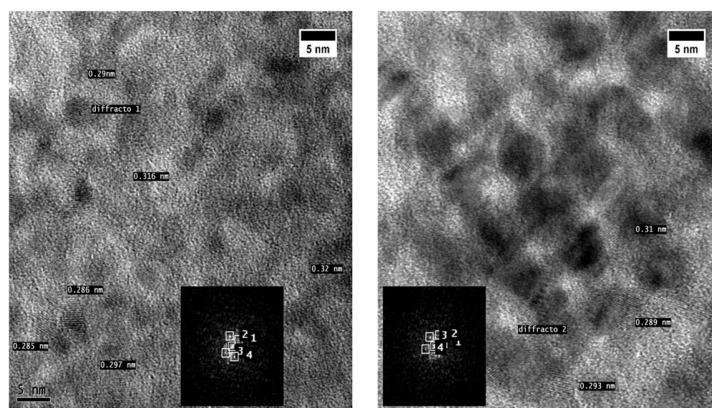
434 **Figure 7.** TEM images obtained for (A, B) NiZr-SBA-IWI, (C, D) NiZr-SBA-TS and (E,
435 F) NiZr-KIT-TS after calcination at 700 °C.

436

437 Finally, images obtained for Ni/meso-Zr are presented in Figure 9. The formation of porous
438 ordered material with pseudo-spherical/cylindrical pores of 8-10 nm in size is observed.
439 The observations fit with the low XRD angle analysis and N₂-physisorption results since
440 they described a material with a poor pore ordering. Finally, in this material, NiO NPs of
441 4.4 ± 1.3 nm average size, aleatory distributed in the ZrO₂ porosity, are observed to form.

442

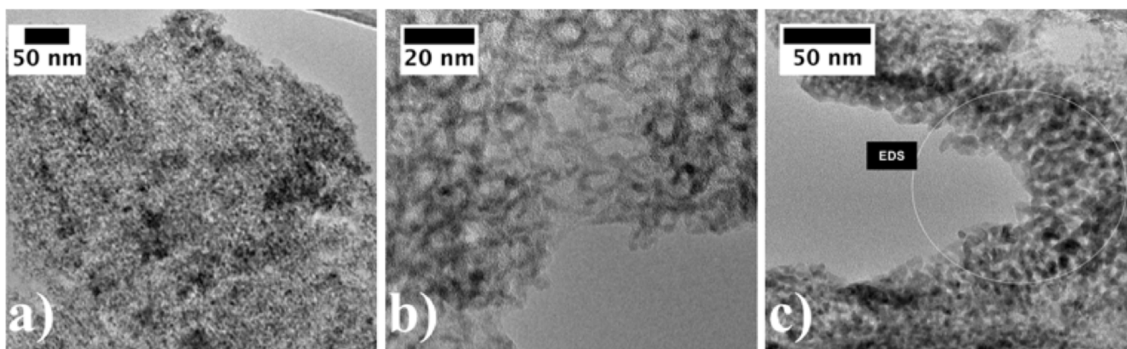
443



444

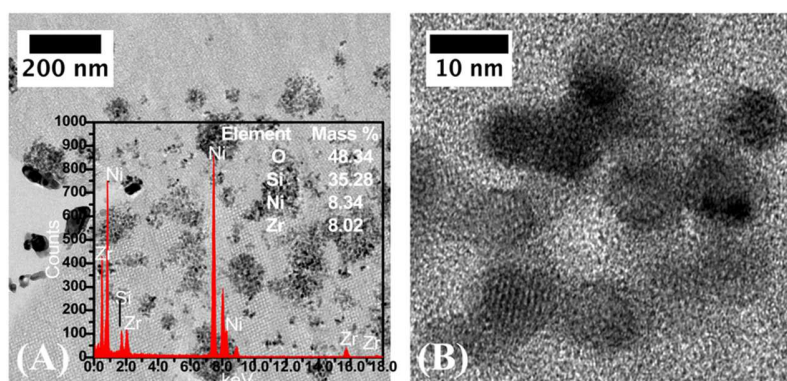
445 **Figure 8.** TEM images of NiZr-KIT-TS sample with particles showing lattice fringes. Fast
446 Fourier transform (FFT) image is shown (inset).

447



448

449 **Figure 9.** TEM images for Ni/meso-Zr after calcination at 700 °C.



450

451 **Figure 10.** TEM images of NiZr-KIT-TS catalyst after reduction at 450 °C for 2 h.

452 Stability of NPs under reducing atmosphere was evaluated for the NiZr-KIT-TS sample,
 453 applying a reduction at 450 °C (pure H₂ at a total flow rate = 50 mL min⁻¹, heating rate of 5
 454 °C min⁻¹) (Fig. 10). No notable evolution of the mesopore confined NPs size (7.2 ± 1.9 nm
 455 for Ni-ZrO₂) and support morphology could be observed after reduction, with the NPs
 456 remaining always confined in mesopores and forming aggregates of sizes ranging from few
 457 tenths of nanometers to one hundred of nanometers. For the external particles, even if few
 458 in proportion, significant sintering was observed, as shown in Figure 10A, selected to show
 459 these rarely observed external particles. From a composition point of view, EDX analysis
 460 revealed the presence of both Ni and ZrO₂ in the particles assemblies of NPs located inside
 461 the silica pores (>100 nm), as observed before reduction. EDX analysis on isolated particles
 462 or few particles assemblies revealed the maintaining of Ni to Zr composition heterogeneity
 463 at the particle level.

464 **3.4. Surface XPS characterization**

465 XPS analysis was carried out to investigate the chemical state of Ni and Zr on the catalysts
 466 surface.

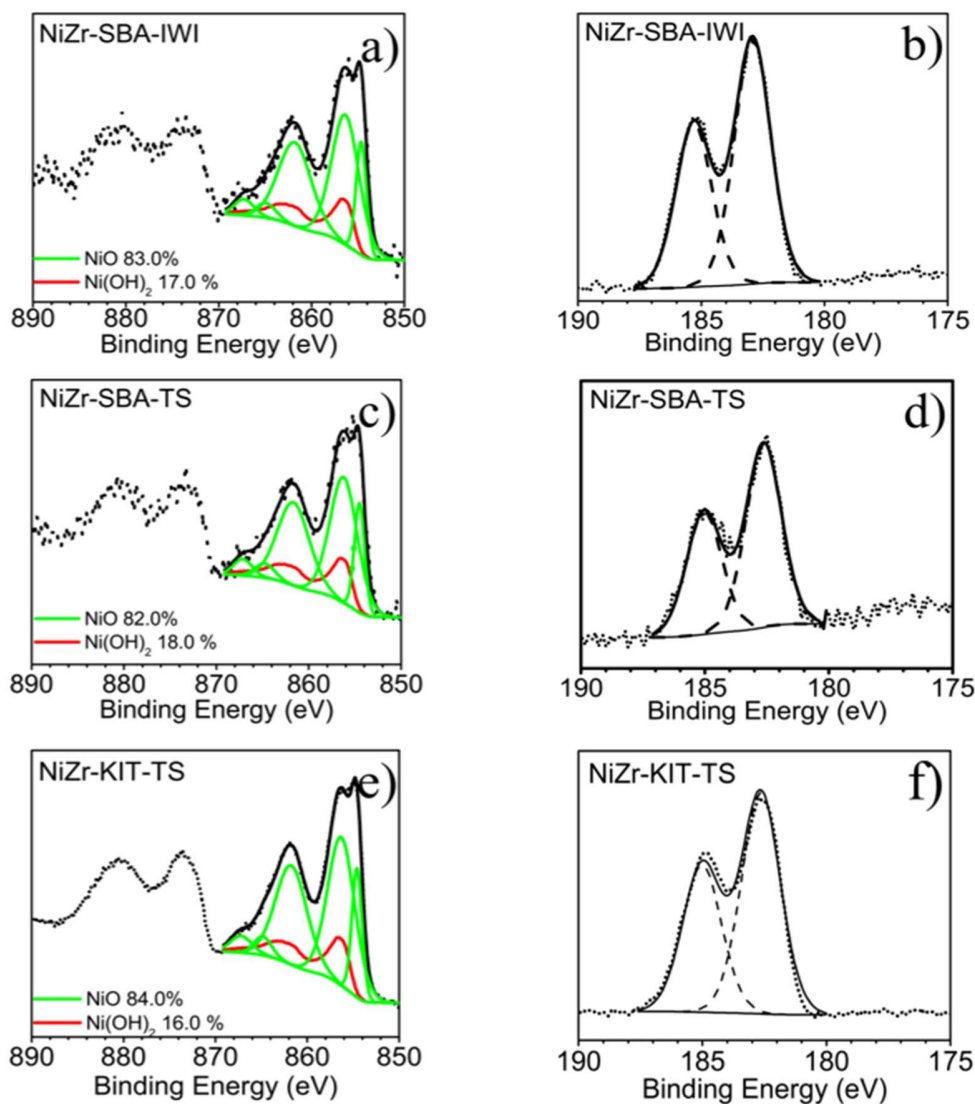
467 *Over silica supported catalysts:* the Ni 2p spectra of catalysts (Fig. 11) exhibited a main Ni
 468 2p_{3/2} signal splitting into two components. Values of the binding energy at ~854-856 eV are
 469 commonly attributed to Ni 2p_{3/2} in NiO species. The multiplet splitting of the main signal
 470 with both maxima being separated from 1.9 eV is also characteristic of NiO formation [91],
 471 in agreement with the phase identified by XRD. Additionally, the Ni 2p spectra, exhibiting
 472 signals at 856.6 ± 0.1 eV, indicated the formation of Ni(OH)₂ species [91]. NiO and

473 Ni(OH)₂ species were then both formed on the catalysts surface, with relative compositions
474 of NiO in the range 82-84% and Ni(OH)₂ in the range 16-18%, independently of the silica
475 support or the impregnation route. The Zr 3d spectra (Fig. 11) showed the doublet peaks of
476 Zr 3d_{5/2} and Zr 3d_{3/2} located at 182.0-182.9 eV and 184.9-185.6 eV, respectively. Binding
477 energies at 182.4 eV and 185.3 eV are commonly reported for Zr in IV oxidation state [92].
478 Then, the results obtained suggested the exclusive presence of Zr(IV) species in the
479 catalysts independently of the silica support type and impregnation route.

480 *Over zirconia catalysts:* Ni 2p spectra also indicated the presence of NiO and Ni(OH)₂
481 species (Fig. 12), with Ni(OH)₂ being the main species (~65%) and NiO the secondary
482 species (~35%). These results demonstrated a higher reactivity of NiO toward
483 rehydroxylation when supported over pure ZrO₂ than over SiO₂. Zr 3d spectra (Fig.12), as
484 for the three silica supported catalysts, indicated the presence of only Zr(IV) species [92,
485 93]. Finally, for this sample, silicon was also quantified by XPS and, as observed by ICP,
486 Si was detected at a concentration of 9.5 at.%. For instance, this result confirmed that the
487 silica hard-template was not completely removed upon NaOH dissolution step.

488

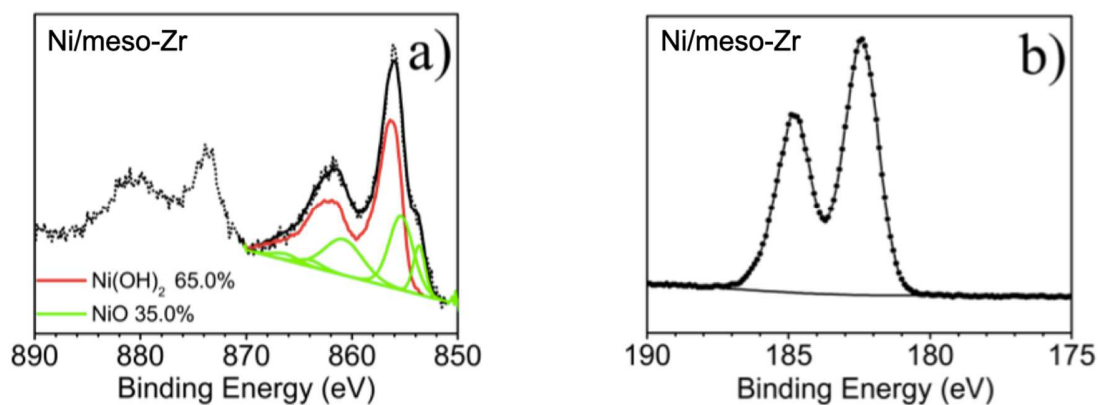
489



490

491 **Figure 11.** XPS Ni 2p spectra for a) NiZr-SBA-IWI, c) NiZr-SBA-TS, e) NiZr-KIT-TS;

492 and XPS Zr 3d spectra for b) NiZr-SBA-IWI, d) NiZr-SBA-TS, f) NiZr-KIT-TS.



493

494 **Figure 12.** a) XPS Ni 2p spectrum and b) XPS Zr 3d spectrum for Ni/meso-Zr.

495

496 3.5. Temperature-programmed reduction (H₂-TPR)

497 NiO reducibility was determined by TPR (Fig. 13). Both NiZr-SBA-IWI and NiZr-SBA-TS
498 samples showed a major hydrogen consumption located between 370-395 °C and a minor
499 one located between 492-520 °C. NiZr-KIT-TS sample exhibited hydrogen consumptions
500 at slightly higher temperatures, centered at 413 °C and 507 °C.

501

502

503

504

505

506

507

508

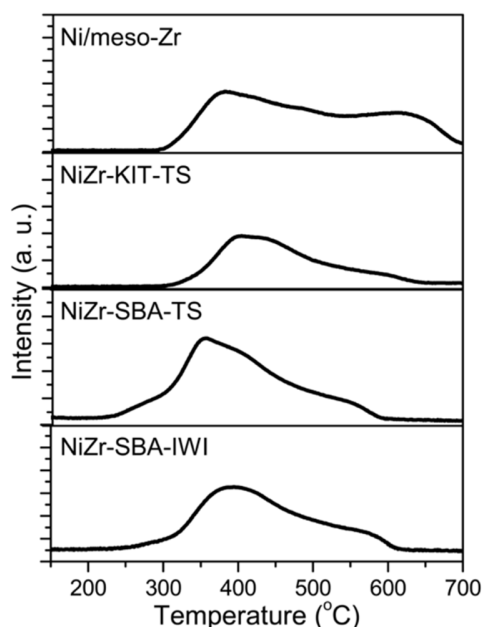
509

510

511

512

513



514 **Figure 13.** Temperature-programmed reduction of NiZr-silica and Ni/meso-Zr samples,
515 after thermal stabilization at 700 °C.

516 Slight differences in reduction temperature can be related to different dispersion degrees, or
517 to the presence of Ni(II) species interacting at different level with SiO₂ surface [94], or
518 even, in our case to Ni(II) interacting with ZrO₂ phase. For instance, the consumptions
519 located at T < 500 °C can be associated to large NiO particles poorly interacting with the
520 support surface and behaving like bulk NiO, while the minor consumptions observed at T >
521 500 °C are associated to the reduction of smaller NiO particles or ionic nickel (Ni(II) ions)
522 in strong interaction with the SiO₂/ZrO₂ surfaces [65, 90, 95]. In the case of Ni/meso-Zr
523 sample, differences with silica-based catalysts are: (i) the shift of the second reduction peak

524 toward higher temperatures (up to a maximum centered at 616 °C); (ii) the increase of this
 525 second peak intensity. Such evolution shows that the proportion of small NiO NPs / NiO in
 526 strong interaction with the support is higher in Ni/meso-Zr than in silica containing
 527 catalysts. The presence of zirconia phase seems to allow a better stabilization of the nickel
 528 ionic species, as already reported [96].

529 **3.6. Temperature-programmed desorption of ammonia (NH₃-TPD)**

530 Acidity of catalysts reduced at 450 °C was measured by NH₃-TPD (Fig. S3). The values of
 531 total acidity of catalysts are gathered in Table 2. The strength of the acidic sites is assigned
 532 according to the desorption temperatures [97-99]: (i) weak acidity, with temperature of
 533 desorption in the <250 °C range; (ii) medium acidity, with desorption between 250 and 400
 534 °C and (iii) strong acidity, for temperature of desorption >400 °C.

535 Desorption profiles obtained for silica supported catalysts exhibited two desorption steps
 536 (Fig. S3a). The first desorption occurred in the temperature range of 150-400 °C, which
 537 characterizes solids of weak to medium acidity strength. Ammonia adsorbed from Lewis
 538 acid sites of the tetragonal zirconia are proposed to desorb at comparable temperature [94].
 539 The second desorption, of lowest intensity, occurred in the 450-700 °C temperature range,
 540 showing the presence of a small proportion of strong acid sites. Ni/SiO₂ powders were not
 541 presenting such strong acidity, ammonia being observed to desorb from only weak acid
 542 sites (at temperatures below 200 °C), while Ni/ZrO₂ exhibited both weak and strong acid
 543 sites [18]. Coordinatively unsaturated sites formed on ionic nickel phase, and acting as
 544 Lewis sites of medium strength, can also contribute to the total acidity [97]. However, as
 545 catalysts were reduced at 400 °C before NH₃-TPD experiments, acidity is expected to
 546 mostly originate from Lewis sites from ZrO₂ surface [100, 101].

547 **Table 2.** Amounts of desorbed NH₃ and surface-normalized quantity obtained for the
 548 reduced catalysts (quantification performed using the m/z = 15 signal).

Sample	Quantity of NH ₃ desorbed (μmol g ⁻¹)	Surface normalized NH ₃ quantity (μmol m ⁻²)
NiZr-SBA-IWI	131	0.37
NiZr-SBA-TS	144	0.39
NiZr-KIT-TS	164	0.37

meso-Zr	81	0.40
Ni/meso-Zr	148	1.1

549

550

551 For meso-Zr (Fig. S3b), a two-step desorption profile was also observed, as in the case of
 552 silica-based catalysts: (i) first desorption from weak to medium acid sites; (ii) second
 553 desorption from strong acid sites. The second peak locates at comparable temperature than
 554 the high temperature desorption obtained on the silica-based catalysts, supporting that the
 555 strong acidity originates well from Lewis sites from the ZrO₂ surface. Ni/meso-Zr
 556 presented comparable two-step desorption, with a shift of the second desorption peak
 557 toward lower temperature by 148 °C. The quantity of ammonia desorbed was multiplied by
 558 a factor of 1.8 between meso-Zr and Ni/meso-Zr (Table 2). Then, the nickel phase
 559 contributes to the global acidity of the material, for the low/intermediate strength acidity,
 560 despite the catalyst was reduced. However, considering that 450 °C is not enough high to
 561 achieve a complete reduction of NiO (Fig. 13), nickel oxidized species acting as Lewis acid
 562 sites remained on the meso-ZrO₂ support.

563 The total acidity of catalysts followed the order NiZr-KIT-TS > Ni/meso-Zr > NiZr-SBA-
 564 TS > NiZr-SBA-IWI, with a difference of only 25% in the total amount of ammonia
 565 desorbed between the less acidic catalyst (NiZr-SBA-IWI) and the more acidic catalyst
 566 (NiZr-KIT-TS). Zirconia phase being more acidic than silica [102], the significant acidity
 567 generated in the silica composites is associated to the efficient dispersion of the ZrO₂ phase
 568 on the mesostructured silica supports. Despite a low loading in ZrO₂, the consequent
 569 surface generated by the dispersed phase of zirconia contributed to the acidity, which
 570 comes in addition to weak to medium acidity of silica. When normalized per surface unit,
 571 difference in acidity between ZrO₂ and SiO₂ catalysts becomes visible (Table 2):

- 572 - All silica supported Ni-ZrO₂ catalysts presented desorbed quantity of 0.38±0.1 μmol m⁻².
 573 Neither the support type (SBA-15 or KIT-6) nor the impregnation route (IWI or TS) has
 574 a significant effect on the material acidity;
- 575 - Ni/meso-ZrO₂ catalyst presented a 2.8 times higher acidity, with 1.10 μmol m⁻² NH₃
 576 desorbed.

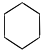
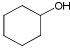
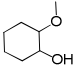
577 3.7. Catalytic performance in HDO of guaiacol

578 **3.7.1. Activity of catalysts**

579 Before reaction, all catalysts were reduced at 450 °C. As a common result of catalytic tests,
 580 analysis of the gas phase indicated the formation of CH₄. Methanol already observed to
 581 form in previous studies [103] was not detected. Gibbs free energies for reactions of
 582 methane and methanol production suggest a favored formation of methane (see ESI file,
 583 section devoted to gas phase analysis). Preliminary tests, performed without catalyst at 300
 584 °C under 5 MPa of H₂, demonstrated a 4% guaiacol (GUA) conversion without detection of
 585 identified reaction products presented in Table 3 (cyclohexane, cyclohexanol and
 586 methoxycyclohexanol). Below, results of the analysis of the liquid phase are presented and
 587 results of the analysis of the gas phase are presented in the supporting information.

588

589 **Table 3.** Catalytic properties of silica and zirconia-based nickel catalysts in the guaiacol
 590 HDO reaction (time of reaction = 8 h, reaction performed at 300 °C under 5 MPa of H₂).

Catalyst	C _{GUA} (%) [*]	Product yield (%)				C _{balance} (%)
					Other	
SBA-15	34	0	0	0	0	90.8
KIT-6	24	0	0	0	0	90.0
NiZr-SBA-IWI	47	5.2	0.7	2.3	29.5	94.5
NiZr-SBA-TS	88	63.5	3.9	0.0	10.6	90.0
NiZr-KIT-TS	93	71.6	3.7	1.6	5.6	89.4
Ni/meso-Zr	100	7.8	43.0	18.0	2.8	71.6
Ni/ZrO₂	86	1.6	40.0	19.9	4.2	79.6

591

592 *Case of silica supported catalysts:* Preliminary experiments performed with silica alone,
 593 SBA-15 and KIT-6, showed GUA conversion of 34% and 24%, respectively. However, no
 594 products among those listed in Table 3 can be detected. TG-DSC analysis performed over
 595 SBA-15 after test showed a carbon total weight loss of 15 wt.% (exothermic decomposition
 596 in the 180-600 °C temperature range). Then, no HDO occurs over silica alone and
 597 consumption of GUA is only related to side reactions and to organic matter accumulation
 598 on the silica surface. With silica supported Ni-ZrO₂ catalysts, under the selected conditions
 599 of temperature and pressure, carbon balances ≥ 89% are always obtained (Table 3),

600 indicating that formation of sub-products through side reactions becomes limited. When
601 reaction is performed with NiZr-SBA-IWI catalyst, GUA conversion of 47% with a yield
602 toward cyclohexane of 5.2% is obtained. Major reaction products remain oxygenated
603 molecules: 1-methyl-1,2-cyclohexanediol, cyclohexanone and methoxycyclohexanone,
604 listed in the 'other' column in Table 3. Significant higher conversion is obtained with the
605 NiZr-SBA-TS catalyst, with GUA conversion reaching 88%. In addition, yield to
606 cyclohexane significantly increased, reaching 63.5% (Table 3). Improvement of yield
607 toward deoxygenated and hydrogenated product demonstrates the better activity of TS-
608 derived catalyst for C-O bond cleavage and C=C/C=O bond hydrogenation. Using 3D KIT-
609 6 support (NiZr-KIT-TS) instead of 2D SBA-15 (NiZr-SBA-TS) allowed to reach slightly
610 higher GUA conversion, 93%, with yield toward cyclohexane reaching 71.6%.
611 Consequently, TS method is far more appropriate to prepare efficient HDO catalyst, since
612 the approach favor the formation of ZrO₂ and Ni particles confined inside the porous hosts.
613 Confining induces an improved proximity between Ni and ZrO₂ surface, both sites in close
614 proximity being necessary for achieving a high selectivity into deoxygenated products
615 during reaction [83, 97, 103]. Acidic properties seem however less important than
616 proximity between the two phases since large differences in HDO efficiencies are obtained
617 between IWI and TS derived catalysts while the global acidity/surface acid site density, as
618 determined by NH₃-TPD, are comparable (Table 2, Fig. S3). Finally, the 3D mesopore
619 structure present in the KIT-6 support is expected to be favorable for the diffusion of
620 reactants/products inside the catalyst, which is reflected by a higher reaction rate than using
621 SBA-15, with no alteration of the yield into deoxygenated molecules.

622 *Case of zirconia supported catalysts:* Using Ni/meso-Zr catalyst, total conversion of GUA
623 was obtained after 8 h of reaction (300 °C, 5 MPa H₂), showing that the catalyst is active. A
624 catalyst of comparable Ni loading prepared over conventional ZrO₂, listed as Ni/ZrO₂ in
625 Table 3, showed lower conversion (86%, Table 3). It demonstrates the beneficial effect of
626 the porosity developed in the meso-Zr support on the Ni dispersion. As compared with
627 SiO₂-supported catalysts, ZrO₂-supported catalysts were significantly less efficient for the
628 complete deoxygenation of GUA. Main products formed were cyclohexanol (~40% yields)
629 and methoxycyclohexanol (~20% yields), while the SiO₂-supported catalysts afforded the
630 production of cyclohexane with yields reaching 71.6% in the best case (Table 3). In

631 addition, incomplete carbon balance is obtained, of only 71.6% with Ni/meso-Zr and 79.6%
632 with Ni/ZrO₂, suggesting the accumulation of polymerization products / coke on the
633 catalyst surface during the reaction. This hypothesis was confirmed performing a TG-DSC
634 analysis over Ni/meso-Zr after 8 h reaction. The results showed a total weight loss of 24.9
635 wt.% in the temperature range of 100-600 °C (Fig. S4), with a step of organic matter
636 decomposition accounting for 12 wt.% at ~300°C. The more important accumulation of
637 carbon species over ZrO₂ support can be associated to its higher surface acidity [104] than
638 that of silica (only ~6 wt.% loss during the decomposition step is observed for SBA-15
639 supported catalyst). A two times higher surface acid site density was indeed measured by
640 NH₃ adsorption (Table 2).

641 Then, the comparison between Ni catalysts supported over ZrO₂ and Ni-ZrO₂ catalysts
642 supported over silica demonstrated the importance of maintaining a high level of dispersion
643 of the zirconia phase to obtain high yields in cyclohexane. Ni however remains active for
644 hydrogenation no matter its environment (supported over silica or over zirconia). On the
645 contrary, bulk ZrO₂ as support for nickel promoted the formation of hydrogenated and
646 partially deoxygenated molecules: high yield to cyclohexanol was obtained (~40%), and
647 side reactions are promoted (with a carbon balance of ~70-80%). When ZrO₂ remains in a
648 divided state over SiO₂, confined in the mesopores and in close proximity of Ni NPs,
649 catalyst becomes more efficient for complete deoxygenation of GUA: 60-70% yields to
650 cyclohexane is obtained with ~90% carbon balance. Proximity between Ni NPs and ZrO₂
651 NPs is consequently a key parameter to maximize hydrodeoxygenation degree of GUA, as
652 already observed for other molecules [18, 83, 97].

653 The presence of metal particles nearby to defect sites of zirconia surface has been suggested
654 to catalyze both deoxygenation and hydrogenation reactions [21, 35, 38]. Cyclohexane
655 formation involves hydrogenolysis of C-O bonds, C=C hydrogenation, and C=O
656 hydrogenation followed by dehydration. Adsorption that occurs on the oxophilic or acidic
657 sites with a flat adsorption configuration could be in favor of the C=C/C=O bond
658 hydrogenation on the metallic sites as well as activation of C-O bond. Results of NH₃-TPD
659 (Table 2) probing only the total acidity of the catalyst, do not allow to confirm this
660 interpretation: Ni/meso-Zr exhibiting the highest density of Lewis acid sites (Table 2) is
661 less efficient for C-O bond cleavage, high yields in cyclohexanol (~40%) and

662 methoxycyclohexanol (~20%) being obtained. Consequently, there is no direct correlation
 663 between the quantity of acidic sites and HDO efficiency, as already observed [18, 105] and
 664 a cooperation between silanol groups on SiO₂ and sites located on ZrO₂ could favor a
 665 proper flat adsorption of GUA and its intermediates for activation of the C-O bonds and
 666 hydrogenation of C=C/C=O bonds.

667 Table 4 presents some key results on the GUA HDO over transition metal-based catalysts.
 668 The catalytic results presented in this work using silica-based supports are among the best
 669 reported for nickel catalysts, especially considering that most interesting results from Table
 670 4 are obtained for Ni-doped catalysts (e.g. NiFe, NiCu based formulations). Metallic nickel
 671 combined with finely divided ZrO₂ on a mesoporous support, especially with a 3D
 672 mesoporous structure, then afford high selectivity in cyclohexane.

673

674 **Table 4.** Catalytic performance of different Ni-, Cu-, Co-, Fe-, Mo-, and ZrO₂-based
 675 catalysts for HDO of guaiacol.

Catalyst	Catalyst amount	Metal loading	[GUA]	P	T (°C)	t (h)	X _{GUA} (%)	Cycl.	Meth.	Cyc-ol	Ref.
NiCu/ZrO ₂ -SiO ₂	1.5 g	Cu: 5 wt.% Ni: 15 wt.%	10 g/100 g solvent	5MPa/H ₂	300	8	100	S=80.8	---	---	[96]
Ni/HZSM-5	0.05 g	15 wt.%	0.28 mol/L	5MPa/H ₂	250	4	100	Y=79	0	0	[106]
Ni/HZSM-5	0.05 g	20 wt%	1 g	30bar/H ₂	200	2	17.8	---	Y=3.1	Y=3.8	[107]
Ni/CNT	200 mg	15 wt.%	0.232 mol/L	5MPa/H ₂	300	4	100	Y=45	Y=5.8	Y=33.3	[108]
Ni&ZrO ₂	0.25 g	---	1.2 g/25 mL	4MPa/H ₂	300	4	82	Y=44	---	Y=70	[109]
NiCo/Al ₂ O ₃	2 wt.%	Ni: 10 wt.% Co:10 wt.%	5 g/45 g solvent	5MPa/H ₂	200	8	96	Y=0.35	---	Y=68.1	[110]
Ni ₅ -Fe ₁ /CNT	100 mg	total 6.59 wt%	WLHSV=60 h ⁻¹	3MPa/H ₂	300	---	96.8	S=83.4	---	S=12.7	[111]
NiMo/SBA-15	2 g	NiO: 6 wt% MoO ₃ : 30 wt%	40 g (3wt.%)	5MPa/H ₂	250	3	90	S=55.8	S=6.7	S=6.3	[112]
Ni/SiO ₂ -ZrO ₂	1.5 g	---	10 g/100 g solvent	5MPa/H ₂	300	8	100	S=96.8	---	---	[113]
Ni/SiO ₂ + β(12.5)	50 mg + 50 mg	---	0.10 g/10 mL solvent	3MPa/H ₂	140	5	>99	Y=55.6	Y=29.7	Y=0.8	[114]
Ni/SiO ₂ + Hβ(50)	50 mg + 50 mg	---	0.10 g/10 mL solvent	3MPa/H ₂	140	2.5	>99	Y=91.7	---	---	[114]
NiZr-1/CMK-3	0.1 g	Ni: 9.2 wt% Zr: 15.9 wt%	0.6 mol/L	5MPa/H ₂	300	8	100	S=30.3	S=16.4	S=47.9	[83]
NiZr-SBA-TS	0.1 g	Ni: 11.0 wt% Zr: 10.6 wt%	0.6 mol/L	5MPa/H ₂	300	8	88	Y=63.5	Y=0.0	Y=3.9	a
NiZr-KIT-TS	0.1 g	Ni: 9.7 wt% Zr: 11.4 wt%	0.6 mol/L	5MPa/H ₂	300	8	93	Y=71.6	Y=1.6	Y=3.7	a

676

a. This work

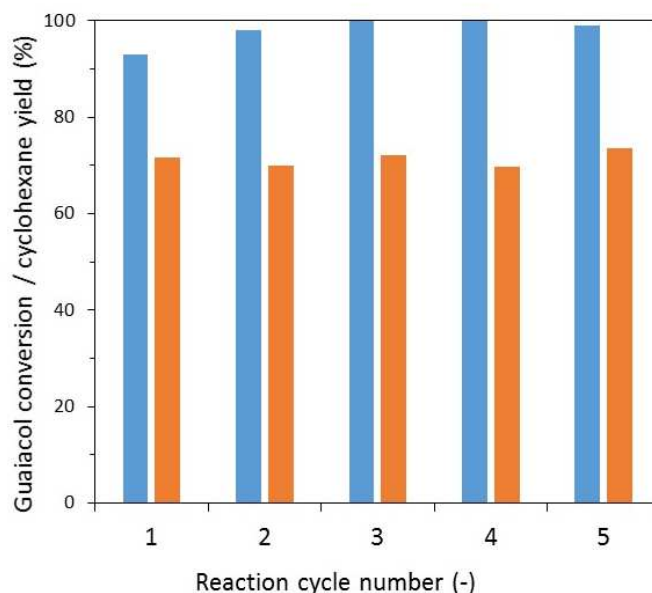
677

Cycl.: cyclohexane, Meth.: methoxycyclohexanol, Cyc-ol.: cyclohexanol, Y: yield (%), S: selectivity (%)

678

679 3.7.2. Stability of catalysts

680 Stability of catalyst was evaluated by recyclability tests performed over NiZr-KIT-TS (Fig.
681 14).



682

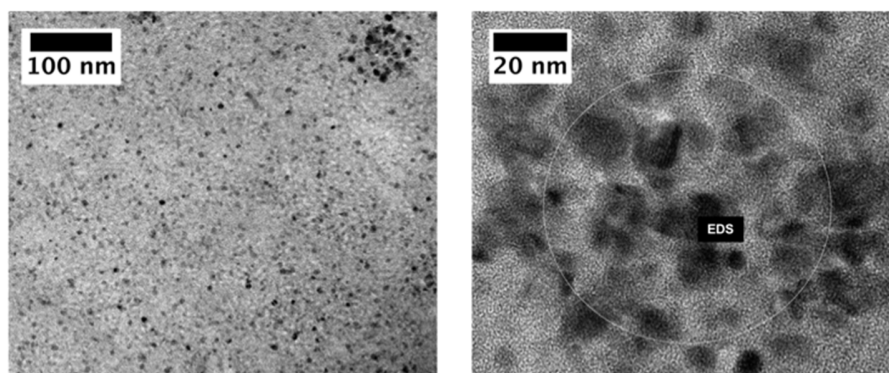
683 **Figure 14.** Recyclability tests performed with NiZr-KIT-TS catalyst (reaction performed at
684 300 °C for 8 h). Blue bars: guaiacol conversion; Orange bars: cyclohexane yields

685

686 Between two cycles, the catalyst was recovered by filtration before being washed with
687 acetone and hexane, dried at 100 °C for 12 h. After recovery of the catalyst, a calcination
688 step is applied in order to remove all adsorbed molecules from the surface (700 °C during 1
689 h). The catalyst is thereafter reduced at 450 °C, and the mass of GUA was adjusted to the
690 mass of the catalyst recovered, without modifying the volume of the solvent, for keeping
691 constant the GUA/catalyst ratio. Results evidenced a satisfying stability, with conversion
692 observed to slightly increase (from 93% to >98%). Minor variations in cyclohexane yield
693 are observed between the successive cycles, oscillating at $70\pm 3\%$, confirming the absence
694 of significant deactivation of catalyst. The stability of the catalyst structure was confirmed
695 by post-reaction characterization (Fig. 15 left). The TEM analysis allowed to observe the
696 well-defined pore structure of the silica support. Then, silica porosity is not significantly
697 modified by the reaction and reactivation procedure. In addition, the active phase remains

698 in the form of confined nanoparticles, mostly located inside the mesopores, with particle
699 size close to those obtained before reaction. Only very few external particle aggregates
700 were found, and even on these external aggregates (Fig. 15 right) the particles remained of
701 low size (<20 nm). On the basis of these observations, and with the maintaining of high and
702 comparable yield in cyclohexane during successive cycles, limited changes in Ni and ZrO₂
703 dispersion and proximity are awaited between successive cycles.

704
705
706
707
708

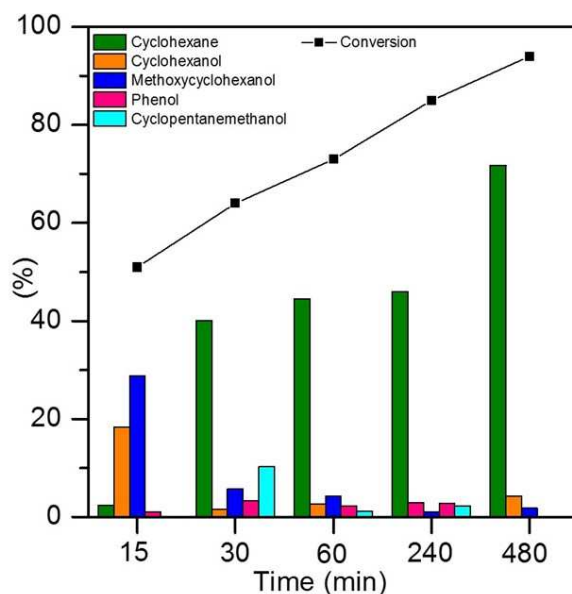


709 **Figure 15.** TEM images of NiZr-KIT-TS catalyst recovered after the 5th catalytic cycle,
710 calcined at 700 °C and further reduced at 450 °C for 2 h.

711

712 3.7.3. Conversion route description

713 Evolution of conversion and product yields with reaction time is presented for NiZr-KIT-
714 TS catalyst in Figure 16. After 15 min of reaction, conversion of GUA reached 51% with a
715 28.8% yield toward methoxycyclohexanol. Lower yields in cyclohexanol and cyclohexane,
716 of 18.3% and 2.4% respectively, are obtained. The main products formed are consequently
717 hydrogenated molecules, indicating as previously described, that Ni is an excellent
718 hydrogenation catalyst. After 30 min reaction, GUA conversion reached 64% and the yields
719 underwent significant changes since the main product formed becomes cyclohexane with a
720 40.1% yield. Secondary products were cyclopentanemethanol, methoxycyclohexanol and
721 cyclohexanol with yields of 10.3 %, 5.8% and 1.5%, respectively. Gradually increasing the
722 reaction time to 8 h leads to an increase in GUA conversion, to reach 94%, and with
723 cyclohexane yield increasing to 71.6% at the expense of the partially deoxygenated
724 products. The presence of cyclohexane, and the absence of aromatics (benzene) detection is
725 showing that dehydrogenation reactions are not favored under the reaction conditions
726 (intermediate temperature of 300 °C and high hydrogen pressure of 5 MPa).



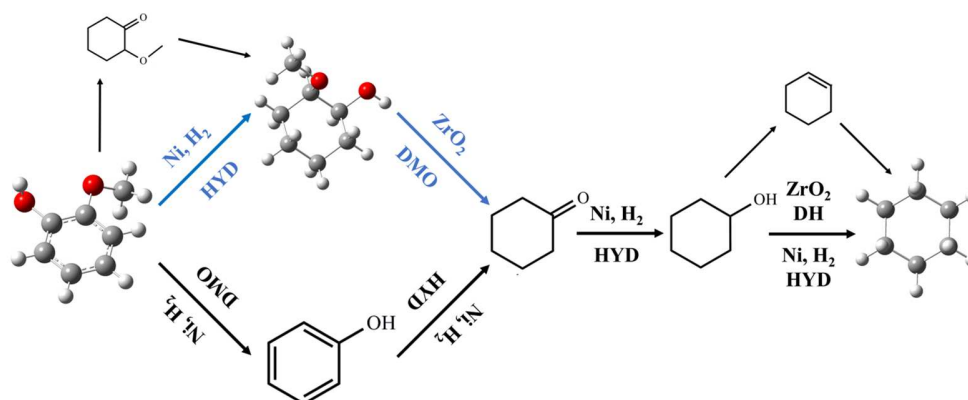
727

728 **Figure 16.** Evolution of conversion and product yields with reaction time over NiZr-KIT-
 729 TS catalyst (reaction performed at 300 °C).

730

731 As observed in Figure 16 at low reaction time, GUA conversion leads to oxygenated
 732 intermediates, prior to the formation of cyclohexane. In order to better elucidate the
 733 primary products of the reaction, reaction was performed decreasing the amount of catalyst
 734 (to 20 mg) and increasing the concentration of GUA (up to 15 wt.%), keeping constant the
 735 other reaction parameters. Products of the reaction were evaluated at 5 and 10 min reaction
 736 time. After 5 min of reaction under these modified conditions, limited GUA conversion is
 737 obtained (16%) and the main products formed were methoxycyclohexanol, phenol,
 738 cyclohexanol and cyclohexanone with 7.0%, 5.6%, 1.6% and 1.0% yields, respectively.
 739 After 10 min reaction, GUA conversion increased to 28% with main reaction products
 740 being methoxycyclohexanol, phenol, methoxycyclohexanone, cyclohexanol and
 741 cyclohexanone with 9.8%, 7.8%, 4.6%, 2.7% and 1.2% yields, respectively. These results
 742 suggest that methoxycyclohexanol and phenol are primary products obtained from GUA
 743 transformation, as represented in Scheme 1. According to these results, guaiacol is expected
 744 to adsorb in different configurations on the catalyst surface: (i) through the aromatic ring on
 745 ZrO₂ sites, on flat π -adsorption configuration allowing the hydrogenation (HYD way) on
 746 the close metallic Ni sites, and thus leading to the formation of methoxycyclohexanol [40,

747 106]; (ii) through the -OH/-OCH₃ groups on ZrO₂ sites, on a flat O-configuration allowing
 748 hydrogenolysis catalysed by Ni particles, allowing the demethoxylation (DMO way)
 749 leading to the formation of phenol [40, 41, 106, 107]. Methoxycyclohexanone was
 750 observed to form at low reaction time. It can be produced by hydrogenation of guaiacol [32,
 751 106]. Its further hydrogenation can lead to methoxycyclohexanol, which can produce
 752 cyclohexanone by demethoxylation.



753

754 **Scheme 1.** Reaction pathway for the hydrodeoxygenation of guaiacol to cyclohexane on
 755 silica supported Ni-ZrO₂ catalysts. HYD: hydrogenation, DMO: demethoxylation, DH:
 756 dehydration.

757

758 The presence of phenol in a first stage of the reaction confirmed that the reaction pathway
 759 included the demethoxylation of GUA to produce phenol, a step followed by the
 760 hydrogenation to produce cyclohexanol via cyclohexanone intermediate [106]. The
 761 presence of methoxycyclohexanol in the first stage of the reaction and the formation of
 762 cyclohexanol prior to cyclohexane confirmed that the reaction pathway also included the
 763 hydrogenation of GUA to produce methoxycyclohexanol, via methoxycyclohexanone
 764 intermediate, a step followed by demethoxylation/hydrogenation to produce cyclohexanol,
 765 via cyclohexanone intermediate. This means that at the beginning of the reaction, carbonyl
 766 products can form but do not remain for a long time in the reaction mixture due to high
 767 activity of the catalyst active phases. Finally, cyclohexanol produces cyclohexane via
 768 dehydration to cyclohexene intermediate, which is likely rapidly hydrogenated as it is not
 769 detected in the reaction medium.

770 **4. Conclusions**

771 Ordered mesoporous SBA-15 and KIT-6 silica materials were used as supports for
772 confining Ni-ZrO₂ active phases. Incipient wetness impregnation (IWI) and two solvents
773 (TS) methods were used for active phase deposition. Ni supported over mesoporous ZrO₂
774 support was also prepared for comparison. The deposition way has a significant influence
775 on catalytic properties of the solid. High conversion of guaiacol is obtained when using the
776 TS approach, with high yield obtained toward cyclohexane (~70%) at high guaiacol
777 conversion degree (~90%). The better performances obtained using the TS approach are
778 ascribed to a better distribution of active zirconia and nickel phases inside the mesopores,
779 and a closer proximity between the Ni and ZrO₂ phases after activation. An additional
780 benefit on the activity is obtained using support with 3-dimensional porosity (KIT-6)
781 instead of 2-dimensional porosity (SBA-15). Finally, excellent stability is reported for silica
782 supported confined Ni-ZrO₂ catalyst with no significant decrease in conversion and yield
783 toward cyclohexane after 5 catalytic cycles. These results are evidences of the efficiency of
784 the confining strategy to produce stable catalyst for HDO reactions. Evolution of
785 conversion and product yields with reaction time over KIT-6 silica supported Ni-ZrO₂
786 particles showed that the hydrogenation and deoxygenation reactions proceeded through the
787 formation of several intermediates, methoxycyclohexanol and phenol being the first
788 detected, which were rapidly converted into cyclohexane. Using Ni supported over
789 mesoporous zirconia led to significantly different catalytic properties. While the guaiacol
790 conversion remained at a high level, reaction yield was oriented toward the production of
791 cyclohexanol (~40%). For instance, it is demonstrated that finely dispersed ZrO₂, in
792 combination with confined Ni NPs, is far more efficient to promote deoxygenation
793 reactions than Ni supported over bulk ZrO₂.

794 **Acknowledgements**

795 The authors acknowledge financial support from the CODI (Comité para el Desarrollo de la
796 Investigación) project "Valorización vía des-oxigenación catalítica de aceites provenientes
797 del tratamiento térmico de biomasa" código (2014-562) University of Antioquia. The
798 authors gratefully acknowledge the University of Antioquia for the "Sostenibilidad"

799 Program. S. Royer and A.-S. Mamede acknowledge Chevreul institute (FR 2638),
800 Ministère de l'Enseignement Supérieur et de la Recherche, Région Nord – Pas de Calais
801 and FEDER for supporting and funding partially this work. S. Royer acknowledges Région
802 Nord-Pas de Calais for UPCAT project funding (Project 15002019).

803 **5. References**

- 804 [1] C. Li, X. Zhao, A. Wang, G.W. Huber, T. Zhang, Catalytic Transformation of Lignin
805 for the Production of Chemicals and Fuels, *Chem. Rev.* 115 (2015) 11559-11624.
- 806 [2] A. Demirbaş, Biomass resource facilities and biomass conversion processing for fuels
807 and chemicals, *Energy Convers. Manage.* 42 (2001) 1357-1378.
- 808 [3] T.V. Choudhary, C.B. Phillips, Renewable fuels via catalytic hydrodeoxygenation,
809 *Appl. Catal., A* 397 (2011) 1-12.
- 810 [4] A.H. Zacher, M.V. Olarte, D.M. Santosa, D.C. Elliott, S.B. Jones, A review and
811 perspective of recent bio-oil hydrotreating research, *Green Chem.* 16 (2014) 491-515.
- 812 [5] G.W. Huber, S. Iborra, A. Corma, Synthesis of Transportation Fuels from Biomass:
813 Chemistry, Catalysts, and Engineering, *Chem. Rev.* 106 (2006) 4044-4098.
- 814 [6] P.M. Mortensen, J.D. Grunwaldt, P.A. Jensen, K.G. Knudsen, A.D. Jensen, A review of
815 catalytic upgrading of bio-oil to engine fuels, *Appl. Catal., A* 407 (2011) 1-19.
- 816 [7] E. Furimsky, Hydroprocessing challenges in biofuels production, *Catal. Today* 217
817 (2013) 13-56.
- 818 [8] D.C. Elliott, T.R. Hart, Catalytic Hydroprocessing of Chemical Models for Bio-oil,
819 *Energy Fuels* 23 (2009) 631-637.
- 820 [9] K. Jacobson, K.C. Maheria, A. Kumar Dalai, Bio-oil valorization: A review, *Renew.*
821 *Sustain. Energy Rev.* 23 (2013) 91-106.
- 822 [10] D.C. Elliott, Biofuel from fast pyrolysis and catalytic hydrodeoxygenation, *Curr. Opin.*
823 *Chem. Eng.* 9 (2015) 59-65.
- 824 [11] I. Sádaba, M. López Granados, A. Riisager, E. Taarning, Deactivation of solid
825 catalysts in liquid media: the case of leaching of active sites in biomass conversion
826 reactions, *Green Chem.* 17 (2015) 4133-4145.
- 827 [12] M. Saidi, F. Samimi, D. Karimipourfard, T. Nimmanwudipong, B.C. Gates, M.R.
828 Rahimpour, Upgrading of lignin-derived bio-oils by catalytic hydrodeoxygenation, *Energy*
829 *Environ. Sci.* 7 (2014) 103-129.
- 830 [13] B. Saha, I. Klein, T. Parsell, M.M. Abu-Omar, Catalytic Hydrodeoxygenation of
831 Lignin Model Compounds, in: M. Schlaf, C.Z. Zhang (Eds.) *Reaction Pathways and*
832 *Mechanisms in Thermocatalytic Biomass Conversion II: Homogeneously Catalyzed*
833 *Transformations, Acrylics from Biomass, Theoretical Aspects, Lignin Valorization and*
834 *Pyrolysis Pathways*, Springer Singapore, Singapore, (2016) 119-129.
- 835 [14] P.M. Mortensen, D. Gardini, H.W.P. de Carvalho, C.D. Damsgaard, J.-D. Grunwaldt,
836 P.A. Jensen, J.B. Wagner, A.D. Jensen, Stability and resistance of nickel catalysts for
837 hydrodeoxygenation: carbon deposition and effects of sulfur, potassium, and chlorine in the
838 feed, *Catal. Sci. Technol.* 4 (2014) 3672-3686.
- 839 [15] C.A. Teles, R.C. Rabelo-Neto, J.R. de Lima, L.V. Mattos, D.E. Resasco, F.B.
840 Noronha, The Effect of Metal Type on Hydrodeoxygenation of Phenol Over Silica
841 Supported Catalysts, *Catal. Lett.* 146 (2016) 1848-1857.

842 [16] M.V. Bykova, S.G. Zavarukhin, L.I. Trusov, V.A. Yakovlev, Guaiacol
843 hydrodeoxygenation kinetics with catalyst deactivation taken into consideration, *Kinet.*
844 *Catal.* 54 (2013) 40-48.

845 [17] E. Furimsky, Catalytic hydrodeoxygenation, *Appl. Catal., A* 199 (2000) 147-190.

846 [18] P.M. Mortensen, J.-D. Grunwaldt, P.A. Jensen, A.D. Jensen, Screening of Catalysts
847 for Hydrodeoxygenation of Phenol as a Model Compound for Bio-oil, *ACS Catal.* 3 (2013)
848 1774-1785.

849 [19] C.A. Teles, R.C. Rabelo-Neto, G. Jacobs, B.H. Davis, D.E. Resasco, F.B. Noronha,
850 Hydrodeoxygenation of Phenol over Zirconia-Supported Catalysts: The Effect of Metal
851 Type on Reaction Mechanism and Catalyst Deactivation, *ChemCatChem* 9 (2017) 2850-
852 2863.

853 [20] P. Sirous-Rezaei, J. Jae, K. Cho, C.H. Ko, S.-C. Jung, Y.-K. Park, Insight into the
854 effect of metal and support for mild hydrodeoxygenation of lignin-derived phenolics to
855 BTX aromatics, *Chem. Eng. J.* (2018) 120121.

856 [21] M. Lu, H. Du, B. Wei, J. Zhu, M. Li, Y. Shan, C. Song, Catalytic Hydrodeoxygenation
857 of Guaiacol over Palladium Catalyst on Different Titania Supports, *Energy Fuels* 31 (2017)
858 10858-10865.

859 [22] D.C. Elliott, Historical Developments in Hydroprocessing Bio-oils, *Energy Fuels*, 21
860 (2007) 1792-1815.

861 [23] A. Popov, E. Kondratieva, L. Mariey, J.M. Goupil, J. El Fallah, J.-P. Gilson, A.
862 Travert, F. Maugé, Bio-oil hydrodeoxygenation: Adsorption of phenolic compounds on
863 sulfided (Co)Mo catalysts, *J. Catal.* 297 (2013) 176-186.

864 [24] V.N. Bui, D. Laurenti, P. Afanasiev, C. Geantet, Hydrodeoxygenation of guaiacol with
865 CoMo catalysts. Part I: Promoting effect of cobalt on HDO selectivity and activity, *Appl.*
866 *Catal., B* 101 (2011) 239-245.

867 [25] P.E. Ruiz, B.G. Frederick, W.J. De Sisto, R.N. Austin, L.R. Radovic, K. Leiva, R.
868 García, N. Escalona, M.C. Wheeler, Guaiacol hydrodeoxygenation on MoS₂ catalysts:
869 Influence of activated carbon supports, *Catal. Commun.* 27 (2012) 44-48.

870 [26] I. Tyrone Ghampson, C. Sepúlveda, R. Garcia, J.L. García Fierro, N. Escalona, W.J.
871 DeSisto, Comparison of alumina- and SBA-15-supported molybdenum nitride catalysts for
872 hydrodeoxygenation of guaiacol, *Appl. Catal., A* 435-436 (2012) 51-60.

873 [27] C. Sepúlveda, K. Leiva, R. García, L.R. Radovic, I.T. Ghampson, W.J. DeSisto, J.L.G.
874 Fierro, N. Escalona, Hydrodeoxygenation of 2-methoxyphenol over Mo₂N catalysts
875 supported on activated carbons, *Catal. Today* 172 (2011) 232-239.

876 [28] Y. Romero, F. Richard, S. Brunet, Hydrodeoxygenation of 2-ethylphenol as a model
877 compound of bio-crude over sulfided Mo-based catalysts: Promoting effect and reaction
878 mechanism, *Appl. Catal., B* 98 (2010) 213-223.

879 [29] T.-R. Viljava, R.S. Komulainen, A.O.I. Krause, Effect of H₂S on the stability of
880 CoMo:Al₂O₃ catalysts during hydrodeoxygenation, *Catal. Today* 60 (2000) 83-92.

881 [30] C. Zhao, Y. Kou, A.A. Lemonidou, X. Li, J.A. Lercher, Highly selective catalytic
882 conversion of phenolic bio-oil to alkanes, *Angew. Chem. Int. Ed. Engl.* 48 (2009) 3987-
883 3990.

884 [31] A. Bjelić, M. Grilc, M. Huš, B. Likozar, Hydrogenation and hydrodeoxygenation of
885 aromatic lignin monomers over Cu/C, Ni/C, Pd/C, Pt/C, Rh/C and Ru/C catalysts:
886 Mechanisms, reaction micro-kinetic modelling and quantitative structure-activity
887 relationships, *Chem. Eng. J.* 359 (2019) 305-320.

888 [32] M. Alda-Onggar, P. Mäki-Arvela, A. Aho, I.L. Simakova, D.Y. Murzin,
889 Hydrodeoxygenation of phenolic model compounds over zirconia supported Ir and Ni-
890 catalysts, *React. Kinet. Mech. Catal.* 126 (2018) 737-759.

891 [33] S. Oh, H.S. Choi, I.-G. Choi, J.W. Choi, Evaluation of hydrodeoxygenation reactivity
892 of pyrolysis bio-oil with various Ni-based catalysts for improvement of fuel properties,
893 *RSC Adv.* 7 (2017) 15116-15126.

894 [34] S. De, J. Zhang, R. Luque, N. Yan, Ni-based bimetallic heterogeneous catalysts for
895 energy and environmental applications, *Energy Environ. Sci.* 9 (2016) 3314-3347.

896 [35] H. Liu, T. Jiang, B. Han, S. Liang, Y. Zhou, Selective phenol hydrogenation to
897 cyclohexanone over a dual supported Pd-Lewis acid catalyst, *Science* 326 (2009) 1250-
898 1252.

899 [36] C. Zhao, J. He, A.A. Lemonidou, X. Li, J.A. Lercher, Aqueous-phase
900 hydrodeoxygenation of bio-derived phenols to cycloalkanes, *J. Catal.* 280 (2011) 8-16.

901 [37] B. Güvenatam, O. Kurşun, E.H.J. Heeres, E.A. Pidko, E.J.M. Hensen,
902 Hydrodeoxygenation of mono- and dimeric lignin model compounds on noble metal
903 catalysts, *Catal. Today* 233 (2014) 83-91.

904 [38] C. Zhao, J.A. Lercher, Upgrading pyrolysis oil over Ni/HZSM-5 by cascade reactions,
905 *Angew. Chem. Int. Ed. Engl.* 51 (2012) 5935-5940.

906 [39] C. Zhao, S. Kasakov, J. He, J.A. Lercher, Comparison of kinetics, activity and stability
907 of Ni/HZSM-5 and Ni/Al₂O₃-HZSM-5 for phenol hydrodeoxygenation, *J. Catal.* 296 (2012)
908 12-23.

909 [40] Y. Berro, S. Gueddida, S. Lebègue, A. Pasc, N. Canilho, M. Kassir, F.E.H. Hassan, M.
910 Badawi, Atomistic description of phenol, CO and H₂O adsorption over crystalline and
911 amorphous silica surfaces for hydrodeoxygenation applications, *Appl. Surf. Sci.* 494 (2019)
912 721-730.

913 [41] R.N. Olcese, M. Bettahar, D. Petitjean, B. Malaman, F. Giovanella, A. Dufour, Gas-
914 phase hydrodeoxygenation of guaiacol over Fe/SiO₂ catalyst, *Appl. Catal., B* 115-116
915 (2012) 63-73.

916 [42] D. Gao, Y. Xiao, A. Varma, Guaiacol Hydrodeoxygenation over Platinum Catalyst:
917 Reaction Pathways and Kinetics, *Ind. Eng. Chem. Res.* 54 (2015) 10638-10644.

918 [43] A.K. Deepa, P.L. Dhepe, Function of Metals and Supports on the Hydrodeoxygenation
919 of Phenolic Compounds, *ChemPlusChem* 79 (2014) 1573-1583.

920 [44] Y. Nakagawa, M. Ishikawa, M. Tamura, K. Tomishige, Selective production of
921 cyclohexanol and methanol from guaiacol over Ru catalyst combined with MgO, *Green*
922 *Chem.* 16 (2014) 2197-2203.

923 [45] A. Gutierrez, R.K. Kaila, M.L. Honkela, R. Slioor, A.O.I. Krause,
924 Hydrodeoxygenation of guaiacol on noble metal catalysts, *Catal. Today* 147 (2009) 239-
925 246.

926 [46] P.M. de Souza, R.C. Rabelo-Neto, L.E.P. Borges, G. Jacobs, B.H. Davis, D.E.
927 Resasco, F.B. Noronha, Hydrodeoxygenation of Phenol over Pd Catalysts. Effect of
928 Support on Reaction Mechanism and Catalyst Deactivation, *ACS Catal.* 7 (2017) 2058-
929 2073.

930 [47] J. Seo, J.S. Kwon, H. Choo, J.-W. Choi, J. Jae, D.J. Suh, S. Kim, J.-M. Ha, Production
931 of deoxygenated high carbon number hydrocarbons from furan condensates:
932 Hydrodeoxygenation of biomass-based oxygenates, *Chem. Eng. J.* 377 (2019).

933 [48] R. Lødeng, C. Ranga, T. Rajkhowa, V.I. Alexiadis, H. Bjørkan, S. Chytil, I.H.
934 Svenum, J. Walmsley, J.W. Thybaut, Hydrodeoxygenation of phenolics in liquid phase
935 over supported MoO₃ and carburized analogues, *Biomass Convers. Bior.* 7 (2017) 343-359.
936 [49] V.O.O. Gonçalves, C. Ciotonea, S. Arrii-Clacens, N. Guignard, C. Roudaut, J.
937 Rousseau, J.-M. Clacens, S. Royer, F. Richard, Effect of the support on the
938 hydrodeoxygenation of m-cresol over molybdenum oxide based catalysts, *Appl. Catal., B*
939 214 (2017) 57-66.
940 [50] Y. Hong, A. Hensley, J.-S. McEwen, Y. Wang, Perspective on Catalytic
941 Hydrodeoxygenation of Biomass Pyrolysis Oils: Essential Roles of Fe-Based Catalysts,
942 *Catal. Lett.* 146 (2016) 1621-1633.
943 [51] A. Berenguer, T.M. Sankaranarayanan, G. Gomez, I. Moreno, J.M. Coronado, P.
944 Pizarro, D.P. Serrano, Evaluation of transition metal phosphides supported on ordered
945 mesoporous materials as catalysts for phenol hydrodeoxygenation, *Green Chem.* 18 (2016)
946 1938-1951.
947 [52] E. Rodríguez-Aguado, A. Infantes-Molina, D. Ballesteros-Plata, J.A. Cecilia, I.
948 Barroso-Martín, E. Rodríguez-Castellón, Ni and Fe mixed phosphides catalysts for O-
949 removal of a bio-oil model molecule from lignocellulosic biomass, *Mol. Catal.* 437 (2017)
950 130-139.
951 [53] Q. Lu, C.-J. Chen, W. Luc, J.G. Chen, A. Bhan, F. Jiao, Ordered Mesoporous Metal
952 Carbides with Enhanced Anisole Hydrodeoxygenation Selectivity, *ACS Catal.* 6 (2016)
953 3506-3514.
954 [54] C. Zhao, Y. Kou, A.A. Lemonidou, X. Li, J.A. Lercher, Hydrodeoxygenation of bio-
955 derived phenols to hydrocarbons using RANEY Ni and Nafion/SiO₂ catalysts, *Chem.*
956 *Commun. (Camb)* 46 (2010) 412-414.
957 [55] X. Zhang, J. Long, W. Kong, Q. Zhang, L. Chen, T. Wang, L. Ma, Y. Li, Catalytic
958 Upgrading of Bio-oil over Ni-Based Catalysts Supported on Mixed Oxides, *Energy Fuels*
959 28 (2014) 2562-2570.
960 [56] P.M. de Souza, R.C. Rabelo-Neto, L.E.P. Borges, G. Jacobs, B.H. Davis, U.M.
961 Graham, D.E. Resasco, F.B. Noronha, Effect of Zirconia Morphology on
962 Hydrodeoxygenation of Phenol over Pd/ZrO₂, *ACS Catal.* 5 (2015) 7385-7398.
963 [57] M. Zaheer, J. Hermannsdörfer, W.P. Kretschmer, G. Motz, R. Kempe, Robust
964 Heterogeneous Nickel Catalysts with Tailored Porosity for the Selective Hydrogenolysis of
965 Aryl Ethers, *ChemCatChem* 6 (2014) 91-95.
966 [58] W. Wang, K. Wu, P. Liu, L. Li, Y. Yang, Y. Wang, Hydrodeoxygenation of p-Cresol
967 over Pt/Al₂O₃ Catalyst Promoted by ZrO₂, CeO₂, and CeO₂-ZrO₂, *Ind. Eng. Chem. Res.* 55
968 (2016) 7598-7603.
969 [59] P.M. de Souza, R.C. Rabelo-Neto, L.E.P. Borges, G. Jacobs, B.H. Davis, T. Sooknoi,
970 D.E. Resasco, F.B. Noronha, Role of Keto Intermediates in the Hydrodeoxygenation of
971 Phenol over Pd on Oxophilic Supports, *ACS Catal.* 5 (2015) 1318-1329.
972 [60] A.M. Robinson, J.E. Hensley, J.W. Medlin, Bifunctional Catalysts for Upgrading of
973 Biomass-Derived Oxygenates: A Review, *ACS Catal.* (2016) 5026-5043.
974 [61] J. Abi Aad, S. Casale, M. Michau, P. Courty, F. Diehl, E. Marceau, X. Carrier,
975 Chemical Weathering of Alumina in Aqueous Suspension at Ambient Pressure A
976 Mechanistic Study, *ChemCatChem* 9 (2017) 2186 – 2194.
977 [62] V.N. Bui, D. Laurenti, P. Delichère, C. Geantet, Hydrodeoxygenation of guaiacol: Part
978 II: Support effect for CoMoS catalysts on HDO activity and selectivity, *Appl. Catal., B* 101
979 (2011) 246-255.

980 [63] P. Sudarsanam, E. Peeters, E.V. Makshina, V.I. Parvulescu, B.F. Sels, Advances in
981 porous and nanoscale catalysts for viable biomass conversion, *Chem. Soc. Rev.* 48 (2019)
982 2366-2421.

983 [64] K. Cassiers, T. Linssen, M. Mathieu, M. Benjelloun, K. Schrijnemakers, P. Van Der
984 Voort, P. Cool, E.F. Vansant, A Detailed Study of Thermal, Hydrothermal, and Mechanical
985 Stabilities of a Wide Range of Surfactant Assembled Mesoporous Silicas, *Chem. Mater.* 14
986 (2002) 2317-2324.

987 [65] A. Ungureanu, B. Dragoi, A. Chiriac, C. Ciotonea, S. Royer, D. Duprez, A.S.
988 Mamede, E. Dumitriu, Composition-Dependent Morphostructural Properties of Ni-Cu
989 Oxide Nanoparticles Confined within the Channels of Ordered Mesoporous SBA-15 Silica,
990 *ACS Appl. Mater. Interfaces* 5 (2013) 3010-3025.

991 [66] A. Galarneau, M. Nader, F. Guenneau, F. Di Renzo, A. Gedeon, Understanding the
992 Stability in Water of Mesoporous SBA-15 and MCM-41, *J. Phys. Chem. C* 111 (2007)
993 8268-8277.

994 [67] C. Gerardin, J. Reboul, M. Bonne, B. Lebeau, Ecodesign of ordered mesoporous silica
995 materials, *Chem. Soc. Rev.* 42 (2013) 4217-4255.

996 [68] J. Kayalvizhi, A. Pandurangan, Hydrodeoxygenation of vanillin using palladium on
997 mesoporous KIT-6 in vapour phase reactor, *Mol. Catal.* 436 (2017) 67-77.

998 [69] R. Olcese, M.M. Bettahar, B. Malaman, J. Ghanbaja, L. Tibavizco, D. Petitjean, A.
999 Dufour, Gas-phase hydrodeoxygenation of guaiacol over iron-based catalysts. Effect of
1000 gases composition, iron load and supports (silica and activated carbon), *Appl. Catal., B* 129
1001 (2013) 528-538.

1002 [70] Y. Yang, G. Lv, L. Deng, B. Lu, J. Li, J. Zhang, J. Shi, S. Du, Renewable aromatic
1003 production through hydrodeoxygenation of model bio-oil over mesoporous Ni/SBA-15 and
1004 Co/SBA-15, *Microporous Mesoporous Mater.* 250 (2017) 47-54.

1005 [71] M.J. Yu, S.H. Park, J.-K. Jeon, C. Ryu, J.M. Sohn, S.C. Kim, Y.-K. Park,
1006 Hydrodeoxygenation of Guaiacol Over Pt/Al-SBA-15 Catalysts, *J. Nanosci. Nanotechnol.*
1007 15 (2015) 527-531.

1008 [72] S. Pichaikaran, A. Pandurangan, Rh/Ni wet-impregnated Ia3d mesostructured
1009 aluminosilicate and r-GO catalysts for hydrodeoxygenation of phenoxybenzene, *New J.*
1010 *Chem.* 41 (2017) 7893-7907.

1011 [73] T.N. Phan, Y.-K. Park, I.-G. Lee, C.H. Ko, Enhancement of CO bond cleavage to
1012 afford aromatics in the hydrodeoxygenation of anisole over ruthenium-supporting
1013 mesoporous metal oxides, *Appl. Catal., A* 544 (2017) 84-93.

1014 [74] D. Zhao, J. Feng, Q. Huo, N. Melosh, G.H. Fredrickson, B.F. Chmelka, G.D. Stucky,
1015 Triblock copolymer syntheses of mesoporous silica with periodic 50 to 300 angstrom pores,
1016 *Science* 279 (1998) 548-552.

1017 [75] D. Zhao, Q. Huo, J. Feng, B.F. Chmelka, G.D. Stucky, Nonionic triblock and star
1018 diblock copolymer and oligomeric surfactant syntheses of highly ordered, hydrothermally
1019 stable, mesoporous silica structures, *J. Am. Chem. Soc.* 120 (1998) 6024-6036.

1020 [76] F. Kleitz, S. Hei Choi, R. Ryoo, Cubic Ia3d large mesoporous silica: synthesis and
1021 replication to platinum nanowires, carbon nanorods and carbon nanotubes, *Chem.*
1022 *Commun.* (2003) 2136-2137.

1023 [77] J. van der Meer, I. Bardez, F. Bart, P.-A. Albouy, G. Wallez, A. Davidson, Dispersion
1024 of Co₃O₄ nanoparticles within SBA-15 using alkane solvents, *Microporous Mesoporous*
1025 *Mater.* 118 (2009) 183-188.

1026 [78] X. Deng, K. Chen, H. Tüysüz, Protocol for the Nanocasting Method: Preparation of
1027 Ordered Mesoporous Metal Oxides, *Chem. Mater.* 29 (2017) 40-52.

1028 [79] V.N.I.o.S.a.T. NIST X-ray Photoelectron Spectroscopy Database, Gaithersburg, 2012;
1029 <http://srdata.nist.gov/xps/>.

1030 [80] H. Wan, R.V. Chaudhari, B. Subramaniam, Catalytic Hydroprocessing of p-Cresol:
1031 Metal, Solvent and Mass-Transfer Effects, *Top. Catal.* 55 (2012) 129-139.

1032 [81] J. He, L. Lu, C. Zhao, D. Mei, J.A. Lercher, Mechanisms of catalytic cleavage of
1033 benzyl phenyl ether in aqueous and apolar phases, *J. Catal.* 311 (2014) 41-51.

1034 [82] J. Ji, H. Guo, C. Li, Z. Qi, B. Zhang, T. Dai, M. Jiang, C. Ren, A. Wang, T. Zhang,
1035 Tungsten-Based Bimetallic Catalysts for Selective Cleavage of Lignin C–O Bonds,
1036 *ChemCatChem* 10 (2018) 415-421.

1037 [83] M. López, R. Palacio, S. Royer, A.-S. Mamede, J.J. Fernández, Mesostructured CMK-
1038 3 carbon supported Ni–ZrO₂ as catalysts for the hydrodeoxygenation of guaiacol,
1039 *Microporous Mesoporous Mater.* 292 (2020).

1040 [84] F. Rouquerol, J. Rouquerol, K.S.W. Sing, G. Maurin, P. Llewellyn, 1 - Introduction,
1041 in: F.R.R.S.W.S.L. Maurin (Ed.) *Adsorption by Powders and Porous Solids* (Second
1042 Edition), Academic Press, Oxford, 2014, pp. 1-24.

1043 [85] D. Gu, C.-J. Jia, C. Weidenthaler, H.-J. Bongard, B. Spliethoff, W. Schmidt, F.
1044 Schüth, Highly Ordered Mesoporous Cobalt-Containing Oxides: Structure, Catalytic
1045 Properties, and Active Sites in Oxidation of Carbon Monoxide, *J. Am. Chem. Soc.* 137
1046 (2015) 11407-11418.

1047 [86] F. Jiao, A.H. Hill, A. Harrison, A. Berko, A.V. Chadwick, P.G. Bruce, Synthesis of
1048 Ordered Mesoporous NiO with Crystalline Walls and a Bimodal Pore Size Distribution, *J.*
1049 *Am. Chem. Soc.* 130 (2008) 5262–5266.

1050 [87] A.R. Menjoge, Q. Huang, B. Nohair, M. Eic, W. Shen, R. Che, S. Kaliaguine, S.
1051 Vasenkov, Combined Application of Tracer Zero Length Column Technique and Pulsed
1052 Field Gradient Nuclear Magnetic Resonance for Studies of Diffusion of Small Sorbate
1053 Molecules in Mesoporous Silica SBA-15, *J. Phys. Chem. C* 114 (2010) 16298-16308.

1054 [88] R. Palacio, J. Gallego, Z. Gabelica, C. Batiot-Dupeyrat, J. Barrault, S. Valange,
1055 Decomposition of ethanol into H₂-rich gas and carbon nanotubes over Ni, Co and Fe
1056 supported on SBA-15 and Aerosil, *Appl. Catal., A* 504 (2015) 642-653.

1057 [89] C. Ciotonea, I. Mazilu, B. Dragoi, C. Catrinescu, E. Dumitriu, A. Ungureanu, H.
1058 Alamdari, S. Petit, S. Royer, Confining for Stability: Heterogeneous Catalysis with
1059 Transition Metal (Oxide) Nanoparticles Confined in the Secondary Pore Network of
1060 Mesoporous Scaffolds, *ChemNanoMat* 3 (2017) 233-237.

1061 [90] C. Ciotonea, B. Dragoi, A. Ungureanu, C. Catrinescu, S. Petit, H. Alamdari, E.
1062 Marceau, E. Dumitriu, S. Royer, Improved dispersion of transition metals in mesoporous
1063 materials through a polymer-assisted melt infiltration method, *Catal. Sci. Technol.* 7 (2017)
1064 5448-5456.

1065 [91] M.C. Biesinger, B.P. Payne, L.W.M. Lau, A. Gerson, R.S.C. Smart, X-ray
1066 photoelectron spectroscopic chemical state quantification of mixed nickel metal, oxide and
1067 hydroxide systems, *Surf. Interface Anal.* 41 (2009) 324-332.

1068 [92] S. Tsunekawa, K. Asami, S. Ito, M. Yashima, T. Sugimoto, XPS study of the phase
1069 transition in pure zirconium oxide nanocrystallites, *Appl. Surf. Sci.* 252 (2005) 1651-1656.

1070 [93] W. Khaodee, B. Jongsomjit, P. Praserttham, S. Goto, S. Assabumrungrat, Impact of
1071 temperature ramping rate during calcination on characteristics of nano-ZrO₂ and its
1072 catalytic activity for isosynthesis, *J. Mol. Catal. A. Chem.* 280 (2008) 35-42.

1073 [94] V.O.O. Gonçalves, P.M. de Souza, T. Cabioc'h, V.T. da Silva, F.B. Noronha, F.
1074 Richard, Hydrodeoxygenation of m-cresol over nickel and nickel phosphide based
1075 catalysts. Influence of the nature of the active phase and the support, *Appl. Catal., B* 219
1076 (2017) 619-628.

1077 [95] J. Ashok, Z. Bian, Z. Wang, S. Kawi, Ni-phyllsilicate structure derived Ni-SiO₂-
1078 MgO catalysts for bi-reforming applications: acidity, basicity and thermal stability, *Catal.*
1079 *Sci. Technol.* 8 (2018) 1730-1742.

1080 [96] X. Zhang, T. Wang, L. Ma, Q. Zhang, Y. Yu, Q. Liu, Characterization and catalytic
1081 properties of Ni and NiCu catalysts supported on ZrO₂-SiO₂ for guaiacol
1082 hydrodeoxygenation, *Catal. Commun.* 33 (2013) 15-19.

1083 [97] O.U. Valdés-Martínez, V.A. Suárez-Toriello, J.A.d.l. Reyes, B. Pawelec, J.L.G. Fierro,
1084 Support effect and metals interactions for NiRu/Al₂O₃, TiO₂ and ZrO₂ catalysts in the
1085 hydrodeoxygenation of phenol, *Catal. Today* 296 (2017) 219-227.

1086 [98] C.V. Loricera, P. Castaño, A. Infantes-Molina, I. Hita, A. Gutiérrez, J.M. Arandes,
1087 J.L.G. Fierro, B. Pawelec, Designing supported ZnNi catalysts for the removal of oxygen
1088 from bio-liquids and aromatics from diesel, *Green Chem.* 14 (2012).

1089 [99] M. Oregui-Bengochea, I. Gandarias, N. Miletić, S.F. Simonsen, A. Kronstad, P.L.
1090 Arias, T. Barth, Thermocatalytic conversion of lignin in an ethanol/formic acid medium
1091 with NiMo catalysts: Role of the metal and acid sites, *Appl. Catal., B* 217 (2017) 353-364.

1092 [100] G. Zhou, J. Liu, X. Tan, Y. Pei, M. Qiao, K. Fan, B. Zong, Effect of Support Acidity
1093 on Liquid-Phase Hydrogenation of Benzene to Cyclohexene over Ru-B/ZrO₂ Catalysts,
1094 *Ind. Eng. Chem. Res.* 51 (2012) 12205-12213.

1095 [101] G. Yang, R. Anumula, H. Luo, Y. Wang, Rationally Positioning Zirconium on
1096 Supported Ru Catalyst for Synergistically Catalytic Upgrading Bio-oil, *Ind. Eng. Chem.*
1097 *Res.* 56 (2017) 13566-13571.

1098 [102] S.-K. Wu, P.-C. Lai, Y.-C. Lin, H.-P. Wan, H.-T. Lee, Y.-H. Chang, Atmospheric
1099 Hydrodeoxygenation of Guaiacol over Alumina-, Zirconia-, and Silica-Supported Nickel
1100 Phosphide Catalysts, *ACS Sustain. Chem. Eng.* 1 (2013) 349-358.

1101 [103] X. Zhang, Q. Zhang, T. Wang, L. Ma, Y. Yu, L. Chen, Hydrodeoxygenation of
1102 lignin-derived phenolic compounds to hydrocarbons over Ni/SiO₂-ZrO₂ catalysts,
1103 *Bioresour. Technol.* 134 (2013) 73-80.

1104 [104] P.-J. Hsu, J.-W. Jiang, Y.-C. Lin, Does a Strong Oxophilic Promoter Enhance Direct
1105 Deoxygenation? A Study of NiFe, NiMo, and NiW Catalysts in p-Cresol Conversion, *ACS*
1106 *Sustain. Chem. Eng.* 6 (2017) 660-667.

1107 [105] P. Zhang, Y. Sun, M. Lu, J. Zhu, M. Li, Y. Shan, J. Shen, C. Song, High-Loading
1108 Nickel Phosphide Catalysts Supported on SiO₂-TiO₂ for Hydrodeoxygenation of Guaiacol,
1109 *Energy Fuels* 33 (2019) 7696-7704.

1110 [106] R.R. Barton, M. Carrier, C. Segura, J.L.G. Fierro, S. Park, H.H. Lamb, N. Escalona,
1111 S.W. Peretti, Ni/HZSM-5 catalyst preparation by deposition-precipitation. Part 2. Catalytic
1112 hydrodeoxygenation reactions of lignin model compounds in organic and aqueous systems,
1113 *Appl. Catal., A* 562 (2018) 294-309.

1114 [107] W. Song, Y. Liu, E. Baráth, C. Zhao, J.A. Lercher, Synergistic effects of Ni and acid
1115 sites for hydrogenation and C-O bond cleavage of substituted phenols, *Green Chem.* 17
1116 (2015) 1204-1218.

1117 [108] A.B. Dongil, I.T. Ghampson, R. Garcia, J.L.G. Fierro, N. Escalona,
1118 Hydrodeoxygenation of guaiacol over Ni/carbon catalysts: effect of the support and Ni
1119 loading, *RSC Adv.* 6 (2016) 2611-2623.

- 1120 [109] X. Zhang, P. Yan, B. Zhao, K. Liu, M.C. Kung, H.H. Kung, S. Chen, Z.C. Zhang,
1121 Selective Hydrodeoxygenation of Guaiacol to Phenolics by Ni/Anatase TiO₂ Catalyst
1122 Formed by Cross-Surface Migration of Ni and TiO₂, ACS Catal. 9 (2019) 3551-3563.
1123 [110] M. Zhou, J. Ye, P. Liu, J. Xu, J. Jiang, Water-Assisted Selective Hydrodeoxygenation
1124 of Guaiacol to Cyclohexanol over Supported Ni and Co Bimetallic Catalysts, ACS Sustain.
1125 Chem. Eng. 5 (2017) 8824-8835.
1126 [111] H. Fang, J. Zheng, X. Luo, J. Du, A. Roldan, S. Leoni, Y. Yuan, Product tunable
1127 behavior of carbon nanotubes-supported Ni-Fe catalysts for guaiacol hydrodeoxygenation,
1128 Appl. Catal., A 529 (2017) 20-31.
1129 [112] B.M.Q. Phan, Q.L.M. Ha, N.P. Le, P.T. Ngo, T.H. Nguyen, T.T. Dang, L.H. Nguyen,
1130 D.A. Nguyen, L.C. Luu, Influences of Various Supports, γ -Al₂O₃, CeO₂, and SBA-15 on
1131 HDO Performance of NiMo Catalyst, Catal. Lett. 145 (2014) 662-667.
1132 [113] X. Zhang, Q. Zhang, L. Chen, Y. Xu, T. Wang, L. Ma, Effect of calcination
1133 temperature of Ni/SiO₂-ZrO₂ catalyst on its hydrodeoxygenation of guaiacol, Chinese J.
1134 Catal. 35 (2014) 302-309.
1135 [114] X. Wang, S. Zhu, S. Wang, Y. He, Y. Liu, J. Wang, W. Fan, Y. Lv, Low temperature
1136 hydrodeoxygenation of guaiacol into cyclohexane over Ni/SiO₂ catalyst combined with H β
1137 zeolite, RSC Adv. 9 (2019) 3868-3876.

1138

1139